Mon. Not. R. Astron. Soc. **337,** 921–937 (2002)

Effects of dust grains on early galaxy evolution

Hiroyuki Hirashita★† and Andrea Ferrara
Osservatorio Astrofisico di Arcetri, Largo Enrico Fermi 5, 50125 Firenze, Italy

Accepted 2002 August 11. Received 2002 July 24; in original form 2002 May 29

ABSTRACT

Stars form out of molecular gas and supply dust grains during their last evolutionary stages; in turn hydrogen molecules (H_2) are produced more efficiently on dust grains. Therefore, dust can drastically accelerate H_2 formation, leading to an enhancement of star formation activity. In order to examine the first formation of stars and dust in galaxies, we model the evolution of galaxies in the redshift range of $5 < z < 20$. In particular, we focus on the interplay between dust formation in Type II supernova ejecta and H_2 production on dust grains. Such effect causes an enhancement of star formation rate by an order of magnitude on a time-scale ($\sim$3–5 galactic dynamical times) shorter than the Hubble time-scale. We also find that about half of the radiative energy from stars is reprocessed by dust grains and is finally radiated in the far-infrared (FIR). For example, the typical star formation rate, FIR and ultraviolet (UV) luminosity of a galaxy with $M_{\rm vir} = 10^{11.5}\,{\rm M}_\odot$ (virial mass) and $z_{\rm vir} = 5$ (formation redshift) are $3\,{\rm M}_\odot\,{\rm yr}^{-1}$, $4 \times 10^9\,{\rm L}_\odot$ and $3 \times 10^9\,{\rm L}_\odot$, respectively. This object will be detected by both the Atacama Large Millimeter Array (ALMA) and the *Next Generation Space Telescope* (*NGST*). Typical star formation rates and luminosities (FIR, UV and metal-line luminosities) are calculated for a large set of ($M_{\rm vir}$, $z_{\rm vir}$). Using these results and the Press–Schechter formalism, we calculate galaxy number counts and integrated light from high-redshift ($z > 5$) galaxies in submillimetre and near-infrared bands. We find that: (i) ALMA can detect dust emission from several $\times\ 10^3$ galaxies per square degree, and (ii) *NGST* can detect the stellar emission from 10^6 galaxies per square degree. Further observational checks of our predictions include the integrated flux of metal (oxygen and carbon) lines; these lines can be used to trace the chemical enrichment and the gas density in early galactic environments. We finally discuss possible colour selection strategies for high-redshift galaxy searches.

Key words: dust, extinction – galaxies: evolution – galaxies: high-redshift – infrared: galaxies – submillimetre.

1 INTRODUCTION

In order to understand the chemical and thermodynamical state of the interstellar medium (ISM) of primeval galaxies, dust formation needs to be considered. Even in metal-poor galaxies, dust grains can drastically accelerate the formation rate of molecular hydrogen (H_2), expected to be the most abundant molecule in the ISM (Hirashita, Hunt & Ferrara 2002a). Hydrogen molecules emit vibrational–rotational lines, thus cooling the gas. This process is particularly important to understand the formation of stars in metal-poor primeval galaxies (e.g. Matsuda, Sato & Takeda 1969; Omukai & Nishi 1998; Nishi & Susa 1999; Bromm, Coppi & Larson 2002; Abel, Bryan & Norman 2002; Nakamura & Umemura 2002; Kamaya & Silk 2002; Ripamonti et al. 2002). The important role of dust on the enhancement of H_2 abundance is also suggested by observations of damped Lyα systems (DLAs; Ge, Bechtold & Kulkarni 2001; cf. Petitjean, Srianand & Ledoux 2000).

The existence of dust in young galaxies is naturally expected because Type II supernovae (SNII) are shown to produce dust grains (e.g. Dwek et al. 1983; Moseley et al. 1989; Kozasa, Hasegawa & Nomoto 1991; Todini & Ferrara 2001). Since the lifetime of SNII progenitors (massive stars) is short, SNII are the dominant production source for dust grains in young ($<$1 Gyr) star-forming galaxies. The winds of evolved low-mass stars contribute to dust formation considerably in nearby galaxies (Gehrz 1989), but the cosmic time is not long enough for such stars to evolve at high redshift ($z > 5$), when all galaxies should have ages smaller than $\sim$1 Gyr. However, dust is also destroyed by SN shocks (McKee 1989; Jones, Tielens & Hollenbach 1996). The detailed modelling of dust evolution in galaxies therefore requires an accurate treatment

★E-mail: irasita@arcetri.astro.it
†Postdoctoral Fellow of the Japan Society for the Promotion of Science (JSPS) for Research Abroad.

of both types of processes (for recent modelling, see e.g. (Edmunds 2001; Hirashita, Tajiri & Kamaya 2002b).

Here we model the evolution of dust content in primeval galaxies. We adopt the results of Todini & Ferrara (2001) for the dust formation rate in SNII. Although further discussion on their application of nucleation theory is necessary (e.g. Frenklach & Feigelson 1997), their results have been successfully applied to the interpretation not only of the properties of SN 1987A but also of the far-infrared (FIR) properties of the young dwarf galaxy SBS 0335−052 (Hirashita et al. 2002a).

One of the most direct observational constraints for the evolution of dust content in galaxies comes from the FIR properties of galaxies. Dust grains absorb stellar light and re-emit it in the FIR. Recent observations by the Submillimetre Common-User Bolometer Array (SCUBA) and the *Infrared Space Observatory* (*ISO*) have made it possible to study galaxy evolution in the FIR band up to $z \lesssim 3$ (Smail et al. 1998). The detection of the cosmic infrared–submillimetre background by the *Cosmic Background Explorer* (*COBE*) (Puget et al. 1996; Fixsen et al. 1998) has also provided crucial information on the star formation history of galaxies in the Universe (e.g. Dwek et al. 1998). Some theoretical works have modelled the FIR evolution of galaxies up to $z \sim 5$ (Tan, Silk & Balland 1999; Pei, Fall & Hauser 1999; Takeuchi et al. 2001a; Xu et al. 2001; Pearson 2001; Totani & Takeuchi 2002), and the FIR luminosity of galaxies per unit comoving volume seems to be much higher at $z \sim 1$ than at $z \sim 0$ (see also Elbaz et al. 2002). However, such a strong 'evolution' beyond $z = 2$ has been excluded (Gispert, Lagache & Puget 2000; Malkan & Stecker 2001; Takeuchi et al. 2001a).

Although there is clear evidence for the existence of dust in galaxies at $z \lesssim 5$ (Armus et al. 1998; Soifer et al. 1998), few works focusing on the early dust formation in galaxies exist. Some 'semi-analytic' works have included dust formation in the early galaxy evolution (e.g. Devriendt & Guiderdoni 2000; Granato et al. 2000), but there has been no study treating dust formation, molecular formation on grain surfaces and star formation history in a consistent manner. Therefore, in this paper, we model the three processes consistently so that we can obtain an observational strategy under a consistent scenario for the early evolution of galaxies.

In order to understand which physical processes govern dust formation, observations at submillimetre wavelengths ($300\ \mu\mathrm{m} \lesssim \lambda \lesssim 1$ mm) are crucial. For high-redshift objects, redshifted FIR radiation (i.e. submillimetre light) should be observed to detect the dust emission. In particular, detecting the submillimetre radiation from galaxies at $z > 5$ requires more sensitive and high-resolution observations (e.g. Takeuchi et al. 2001b). A future ground-based interferometric facility, the Atacama Large Millimeter Array[1] (ALMA), can be used to study such high-redshift galaxies. The detected amount of metals and stars can be used to constrain the galaxy evolution through a chemical evolution model (Tinsley 1980). Redshifted submillimetre metal emission lines can also be observed with ALMA. This can directly constrain the abundance of metals formed in the early epoch of galaxy evolution. [Oh (2002) have also proposed to probe high-redshift intergalactic medium metallicity by metal absorption lines.] In order to detect the stellar light from the high-redshift Universe, observations by the *Next Generation Space Telescope*[2] (*NGST*) in the near-infrared (NIR) will be particularly suitable. At 2 μm, for example, we can observe the ∼2000 Å ultraviolet (UV) light radiated from a galaxy at $z \sim 10$. Therefore, our scenario will become testable in the near future. This means that it is worth constructing a consistent model for high-redshift galaxy evolution.

For any observational facility, statistical properties of galaxies should be discussed to obtain a general picture of galaxy evolution. Two quantities are particularly important for statistical purposes: galaxy number counts (the number of galaxies as a function of observed flux) and integrated light [the sum of the flux from all the galaxies considered; see Hauser & Dwek (2001) for a review]. In this paper, therefore, we estimate the contribution of high-redshift galaxies to these two quantities.

Throughout this paper, we assume a flat cold dark matter (CDM) cosmology with a cosmological constant. The values of quantities are the same as those in Mo & White (2002) ($\Omega_\mathrm{M} = 0.3$, $\Omega_\Lambda = 0.7$ and $H_0 \equiv 100\,h$ km s^{-1} Mpc^{-1} = 70 km s^{-1} Mpc^{-1}). The baryon density parameter is assumed to be $\Omega_\mathrm{b} = 0.02\,h^{-2}$. For the power spectrum of the density fluctuation, $n = 1$ and $\sigma_8 = 0.9$ are adopted. We first model the physical state of the gas and the content of dust and metals in a galaxy during its early evolutionary stage (Section 2). There we also model the luminosities of FIR, UV and metal lines. The results of our model for fiducial galaxies are presented in Section 3. Based on these results, we next calculate the galaxy number counts and the integrated light at various wavelengths in Section 4. We discuss the observational implications of our results in Section 5.

2 GALAXY EVOLUTION MODEL

We aim at modelling the star formation rate during the early stage of galaxy evolution. We consider that stars form only in molecular environments, where cooling to a low temperature is possible. We solve the evolution of molecular content in a way consistent with the star formation history and the dust supply from stars. Some of the past studies (e.g. Norman & Spaans 1996) have also considered similar processes, but we now tie star formation to the molecular content in determining the star formation rate (Section 2.2).

Before $z = 5$, all the galaxies are younger than the cosmic age[3] of 1.2 Gyr. Although dust can play an important role in forming hydrogen molecules, the model for the evolution of dust content in the early epoch of the Universe has not been developed yet. Since planned facilities will enable us to observe dust emission from $z > 5$, it is worth constructing a theoretical framework for the dust evolution at $z > 5$. For observational strategies, we estimate the radiative energy at various wavelengths. For $z > 20$, the number of galaxies that survive stellar feedback is negligible (Ciardi et al. 2000). Therefore, we concentrate ourselves on galaxies formed between $z = 20$ and 5.

2.1 Interstellar medium evolution

2.1.1 Gas density

The star formation process is affected by the physical state of the ISM. In particular, cooling by molecular hydrogen plays an important role in star formation. Although the law governing the galactic star formation rate is not established at all for primeval galaxies [Kennicutt's empirical law is derived from observations of nearby galaxies (Kennicutt 1998)], the abundance of H_2 should be ultimately a key parameter as stars are only seen to form in molecular complexes [see e.g. Wilson et al. (2000) for a recent observation of

[1] http://www.eso.org/projects/alma/
[2] http://ngst.gsfc.nasa.gov/

[3] The cosmic ages for the adopted cosmology at $z = 5$, 10 and 20 are 1.2, 0.47 and 0.18 Gyr, respectively.

a nearby galaxy]. Moreover, enhancement of molecular gas formation is shown to result in active star formation [for recent results, see e.g. Walter et al. (2002)]. We define the molecular fraction of hydrogen, $f_{\rm H_2}$, as

$$f_{\rm H_2} \equiv 2n_{\rm H_2}/n_{\rm H}, \tag{1}$$

where $n_{\rm H}$ and $n_{\rm H_2}$ are the number densities of hydrogen nuclei and hydrogen molecules, respectively (i.e. if all the hydrogen nuclei are in the molecular form, $f_{\rm H_2} = 1$). The importance of $f_{\rm H_2}$ in the star formation law is modelled in Section 2.2.

We consider a pure hydrogen gas, and neglect helium in this paper for the following two reasons. First, helium has little influence on the electron abundance [i.e. the formation rate of H_2 in the gas phase is not affected by the presence of He (Hutchings et al. 2002)]. Secondly, the existence of helium does not affect the temperature of the gas and thus it does not change the reaction rates concerning H_2 formation (Kitayama et al. 2001). In order to examine the time evolution of $f_{\rm H_2}$, we solve a set of reaction equations describing H_2 formation and destruction.

First, we must estimate the number density of the hydrogen gas $n_{\rm H}$, because it affects both the reaction rate and the cooling rate. The objects that can form stars continuously against the heating from interstellar UV (IUV)[4] radiation and stellar kinetic energy input have virial temperature typically larger than 10^4 K (Ciardi et al. 2000). Since we are interested in the star formation activity of galaxies, we only consider objects whose virial temperature is larger than that value. If the gas temperature is larger than 10^4 K, cooling by hydrogen atomic lines is efficient. Then the gas loses pressure and collapses in the gravitational field of dark matter. Even in the presence of UV background radiation, objects with such a high virial temperature can collapse because of efficient cooling and H_2 self-shielding (Kitayama et al. 2001). The collapse increases the H_2 column density further, and, as a result, external UV shielded by H_2 has little effect on the temperature and dynamics of the gas after the collapse. Therefore, we neglect the external UV radiation field.

Since the gas cooling time is much shorter than the Hubble time-scale for the objects of interest in this paper (Madau, Ferrara & Rees 2001), we expect that a significant fraction of baryons finally collapse in the dark matter potential. If the halo is rotating, the gas will collapse in a centrifugally supported disc. The radius ($r_{\rm disc}$) and the scaleheight (H) of the disc are determined following Ferrara, Pettini & Shchekinov (2000) (see also Norman & Spaans 1996; Ciardi & Loeb 2000). By considering the conservation of angular momentum and assuming a typical value for the spin parameter ($\lambda = 0.04$; Barnes & Efstathiou 1987; Steinmetz & Bartelmann 1995), we obtain $r_{\rm disc} \simeq 0.18 r_{\rm vir}$, and the radius of the dark halo, $r_{\rm vir}$, is estimated in terms of the mass of the dark halo, $M_{\rm vir}$, and the redshift of virialization, $z_{\rm vir}$, as

$$\tfrac{4}{3}\pi r_{\rm vir}^3 \Delta_{\rm c} \rho_{\rm c0} \Omega_{\rm M} (1+z_{\rm vir})^3 = M_{\rm vir}, \tag{2}$$

where $\rho_{\rm c0} \equiv 3c^2 H_0^2/8\pi G$ and $\Delta_{\rm c}$ are the critical density of the Universe at $z = 0$ and the overdensity of an object formed at $z_{\rm vir}$, respectively. The spherical collapse model (e.g. Peebles 1980) predicts $\Delta_{\rm c}(z_{\rm vir}) \simeq 180$. We adopt the fitting formula given by Kitayama & Suto (1996) for $\Delta_{\rm c}(z_{\rm vir})$ as

$$\Delta_{\rm c}(z_{\rm vir}) \simeq 18\pi^2 \left[1 + 0.4093 (1/\Omega_{\rm v} - 1)^{0.9052}\right], \tag{3}$$

where $\Omega_{\rm v}$ is the density parameter at $z_{\rm vir}$ given by

$$\Omega_{\rm v} = \frac{\Omega_{\rm M}(1+z_{\rm vir})^3}{\Omega_{\rm M}(1+z_{\rm vir})^3 + (1-\Omega_{\rm M}-\Omega_\Lambda)(1+z_{\rm vir})^2 + \Omega_\Lambda}. \tag{4}$$

This formula is applicable only to a flat universe ($\Omega_{\rm M} + \Omega_\Lambda = 1$) with $\Omega_{\rm M} < 1$.

Using $r_{\rm disc}$ and H (the scaleheight of the disc), $n_{\rm H}$ is estimated from

$$n_{\rm H} \simeq \frac{M_{\rm vir}\Omega_{\rm b}}{\pi r_{\rm disc}^2 2 H m_{\rm H} \Omega_{\rm M}}, \tag{5}$$

where $m_{\rm H}$ is the mass of a hydrogen atom. We have assumed that the mass of a galaxy is dominated by the dark halo and that the mass of the gas is $M_{\rm vir}\Omega_{\rm b}/\Omega_{\rm M}$.

An object collapsed at $z_{\rm vir}$ with a mass of $M_{\rm vir}$ has a virial temperature, $T_{\rm vir}$, defined as

$$T_{\rm vir} \equiv \frac{G\mu M_{\rm vir}}{3 k_{\rm B} r_{\rm vir}}, \tag{6}$$

where G is the gravitational constant, $k_{\rm B}$ is the Boltzmann constant and μ is the mean molecular weight. The factor '3' can be different depending on the radial profile of gas. Therefore, the definition of $T_{\rm vir}$ contains an uncertainty of the order of unity. Since we are considering a pure hydrogen gas, $\mu = (1+x)^{-1} m_{\rm H}$, where x is the ionization degree (fraction of hydrogen nuclei in the ionized state), which is derived from equation (9) below. The circular velocity, $v_{\rm c}$, is defined as

$$v_{\rm c} \equiv \sqrt{\frac{G M_{\rm vir}}{r_{\rm vir}}}; \tag{7}$$

we also define the circular time-scale, $t_{\rm cir}$, as

$$t_{\rm cir} \equiv \frac{2\pi r_{\rm disc}}{v_{\rm c}}. \tag{8}$$

The disc thickness relative to the radius is estimated by using the formalism in Ferrara et al. (2000). Using $T_{\rm vir}$ (equation 6) for the gas temperature, $H/r_{\rm disc}$ is estimated to be $\sim$0.1. We fix this thickness for the disc throughout the time evolution of each galaxy. Probably H could decrease further as gas cools, but it is difficult to include a dynamical evolution of gas into our one-zone model. Moreover, turbulent energy supplied by SNII increases H, an effect that is hard to quantify in the framework of this paper. The resulting gas density roughly follows the scaling relation: $n_{\rm H} \sim 80[(1+z_{\rm vir})/10]^3$ cm^{-3}. This is higher than the typical density of the local interstellar medium ($n_{\rm H} \sim 1$ cm^{-3}), reflecting the high-density environment of the high-redshift Universe. However, that density is lower than that calculated by Norman & Spaans (1996) because of our higher $H/r_{\rm disc}$. Even in our case, the gas cools to reach 300 K on a short ($\sim t_{\rm cir}$) time-scale and star formation becomes possible anyway. The detailed treatment of $H/r_{\rm disc}$ does not affect any of the following conclusions except for the metal-line emission, for which we will discuss the uncertainty caused by this factor (Section 2.5.2). The gas consumption into stars is also neglected. This is a valid assumption in this paper, because in our calculation star formation history is only traced until $\lesssim$30 per cent of the gas content is consumed.

2.1.2 *Chemistry and cooling*

We calculate the time evolution of ionization degree (x), molecular fraction ($f_{\rm H_2}$; equation 1) and gas temperature (T) of the hydrogen gas. The molecular fraction is particularly relevant here, because it

[4]In order to avoid confusion between external (background) and internal (interstellar) UV fields, we call the UV from stars within the galaxy 'IUV'.

Table 1. Reaction rates needed to calculate the abundance of H_2. The unit of the gas temperature T is K unless otherwise stated. References: 1, Omukai (2000); 2, Galli & Palla (1998); 3, this paper.

No.	Reaction	Rate ($cm^3\ s^{-1}$)	Ref.
[1]	$H + e^- \longrightarrow H^+ + 2e^-$	$\exp\{-32.71 + 13.54\ln(T/\mathrm{eV}) - 5.379[\ln(T/\mathrm{eV})]^2 + 1.563[\ln(T/\mathrm{eV})]^3 - 0.2877[\ln(T/\mathrm{eV})]^4 + 3.483\times10^{-2}[\ln(T/\mathrm{eV})]^5 - 2.632\times10^{-3}[\ln(T/\mathrm{eV})]^6 + 1.120\times10^{-4}[\ln(T/\mathrm{eV})]^7 - 2.039\times10^{-6}[\ln(T/\mathrm{eV})]^8\}$	1
[2]	$H^+ + e^- \longrightarrow H + \gamma$	$\exp\{-28.61 - 0.7241[\ln(T/\mathrm{eV})] - 2.026\times10^{-2}[\ln(T/\mathrm{eV})]^2 - 2.381\times10^{-3}[\ln(T/\mathrm{eV})]^3 - 3.213\times10^{-4}[\ln(T/\mathrm{eV})]^4 - 1.422\times10^{-5}[\ln(T/\mathrm{eV})]^5 + 4.989\times10^{-6}[\ln(T/\mathrm{eV})]^6 + 5.756\times10^{-7}[\ln(T/\mathrm{eV})]^7 - 1.857\times10^{-8}[\ln(T/\mathrm{eV})]^8 - 3.071\times10^{-9}[\ln(T/\mathrm{eV})]^9\}$	1
[3]	$H + e^- \longrightarrow H^- + \gamma$	$1.4\times10^{-18}\,T^{0.928}\exp(-T/1.62\times10^4)$	1
[4]	$H^- + H \longrightarrow H_2 + e^-$	$4.0\times10^{-9}\,T^{-0.17}(T>300)$; $\quad 1.5\times10^{-9}(T<300)$	1
[5]	$H^- + H^+ \longrightarrow 2H$	$5.7\times10^{-6}\,T^{-1/2} + 6.3\times10^{-8} - 9.2\times10^{-11}\,T^{1/2} + 4.4\times10^{-13}\,T$	1
[6]	$H + H^+ \longrightarrow H_2^+ + \gamma$	$\mathrm{dex}[-19.38 - 1.523\log_{10}T + 1.118(\log_{10}T)^2 - 0.1269(\log_{10}T)^3]$	1
[7]	$H_2^+ + H \longrightarrow H_2 + H^+$	6.4×10^{-10}	1
[8]	$H_2^+ + e^- \longrightarrow 2H$	$2.0\times10^{-7}\,T^{-1/2}$	1
[9]	$H_2 + H^+ \longrightarrow H_2^+ + H$	$3.0\times10^{-10}\exp(-21\,050/T)(T<10^4)$; $1.5\times10^{-10}\exp(-14\,000/T)(T>10^4)$	2
[10]	$H_2 + H \longrightarrow 3H$	$k_{\mathrm{H}}^{1-a}k_{\mathrm{L}}^{a}$ with $k_{\mathrm{L}} = 1.12\times10^{-10}\exp(-7.035\times10^4/T)$, $k_{\mathrm{H}} = 6.5\times10^{-7}\,T^{-1/2}\exp(-5.2\times10^4/T)[1-\exp(-6000/T)]$, $a = 4.0 - 0.416\log_{10}(T/10^4) - 0.327[\log_{10}(T/10^4)]^2$	1
[11]	$H_2 + e^- \longrightarrow 2H + e^-$	$4.4\times10^{-10}\,T^{0.35}\exp(-1.02\times10^5/T)$	1
dust	$H + H + \mathrm{grain} \longrightarrow H_2 + \mathrm{grain}$	$2.8\times10^{-15}(T/100\,\mathrm{K})^{1/2}$ if $T<300$; 0 if $T>300$ (see Appendix A)	3

Table 2. Cross-sections for photoionization and photodissociation processes. The unit of ν (frequency of light) is Hz. References: 1, Kitayama & Ikeuchi (2000); 2, Abel et al. (1997); 3, Tegmark et al. (1997).

No.	Reaction	Cross-section (cm^2)	ν range (Hz)	Ref.
[12]	$H + \gamma \longrightarrow H^+ + e^-$	$6.30\times10^{-18}(\nu/3.3\times10^{15})^{-3.0}$ effect of optical depth also included in the text	$\nu > 3.3\times10^{15}$	1
[13]	$H_2 + \gamma \longrightarrow H_2^* \longrightarrow 2H$	see equation (17)		2
[14]	$H^- + \gamma \longrightarrow H + e^-$	$3.486\times10^{-16}(x-1)^{3/2}/x^{3.11}$ $[x \equiv \nu/1.8\times10^{14}]$	$\nu > 1.8\times10^{14}$	3
[15]	$H_2^+ + \gamma \longrightarrow H + H^+$	$7.401\times10^{-18}\,\mathrm{dex}(-x^2 - 0.0302x^3 - 0.0158x^4)$ $[x \equiv 2.762\ln(\nu/2.7\times10^{15})]$	$\nu > 6.4\times10^{14}$	3

determines the final cooling rate of gas when stars form ($T \sim 300$ K). In order to determine $f_{\mathrm{H_2}}$, we also calculate T and x. The equations are basically the same as those of Hutchings et al. (2002) except for the photo-processes (reaction of gas with photons from stars) and the formation of H_2 on dust grains. We summarize the reactions considered in this paper and their rate coefficients (R_n; $n = 0, \ldots, 11$) in Table 1. In Table 1, we also list the reaction coefficient for the H_2 formation on dust, R_{dust} (see Appendix A for details; see also Haiman, Rees & Loeb 1996, for the list of important reactions). In Table 2, we list the photo-processes and their cross-sections. The reaction rates of those photo-processes are expressed as Γ_n ($n = 12, \ldots, 15$).

The time evolution of the ionization degree is described as

$$\frac{\mathrm{d}x}{\mathrm{d}t} = x f_0 R_1 n_{\mathrm{H}} - x^2 R_2 n_{\mathrm{H}} + \Gamma_{12} f_0, \tag{9}$$

where $f_0 \equiv 1 - x - f_{\mathrm{H_2}}$ is the neutral fraction of hydrogen. The terms on the right-hand side are the rates of collisional ionization, recombination and photoionization. Next the time evolution of the molecular fraction is written as

$$\frac{\mathrm{d}f_{\mathrm{H_2}}}{\mathrm{d}t} = 2f_0^2 x n_{\mathrm{H}}(R_{\mathrm{eff},1} + R_{\mathrm{eff},2}) + 2R_{\mathrm{dust}}\mathcal{D}n_{\mathrm{H}}f_0 - f_{\mathrm{H_2}}n_{\mathrm{H}}\left(x^2 R_{\mathrm{eff},3} + f_0 R_{10} + x R_{11}\right) - \Gamma_{13} f_{\mathrm{H_2}}, \tag{10}$$

where

$$R_{\mathrm{eff},1} \equiv \frac{R_3 R_4}{f_0 R_4 + x R_5 + \Gamma_{14}/n_{\mathrm{H}}}, \tag{11}$$

$$R_{\mathrm{eff},2} \equiv \frac{R_6 R_7}{f_0 R_7 + x R_8 + \Gamma_{15}/n_{\mathrm{H}}} \tag{12}$$

are the effective formation rates of H_2 including the effect of destruction rate of H^- and H_2^+, respectively, and

$$R_{\mathrm{eff},3} \equiv \frac{R_9 R_8}{f_0 R_7 + x R_8 + \Gamma_{15}/n_{\mathrm{H}}} \tag{13}$$

is the destruction of H_2^+ due to H^- collisions. On the right-hand side of equation (10), we estimate the rates of the formation in the gas phase, destruction via reactions [9]–[11] of Table 1, photodissociation and formation on grains ($\mathcal{D}$ is the dust-to-gas mass ratio). We also list the H_2 formation rate on grains, R_{dust}, in Table 1 (the details are given in Appendix A). The treatment of photoionization

and H_2 photodissociation rates is described in the next paragraph. For the initial conditions on x and f_{H_2} at $t = 0$ ($z = z_{vir}$), we assume the equilibrium values determined by T_{vir} and n_H. The result is, however, insensitive to the choice of these values, and as gas cools the molecular fraction always reaches $f_{H_2} \sim$ a few $\times 10^{-3}$ by $t \sim 10^7$ yr, when the electron abundance becomes too small to produce further H_2 in the gas phase.

Equation (A20) of Kitayama & Ikeuchi (2000) gives Γ_{12} (Γ_{HI} in their notation) as a function of the incident UV intensity and the H I column density. Although derived for background UV radiation, their formula is applicable to the IUV field as well. We assume that the photon paths are optically thin against ionization of H^- and dissociation of H_2^+. We also use their equation (A21) to estimate the photoionization heating. The effect of radiative transfer is included for photons ionizing H in the form of the column density of H I, N_{HI}. We estimate the column density by $N_{HI} \simeq n_H(1 - x - f_{H_2})r_{disc}$. In order to use the formulation by Kitayama & Ikeuchi (2000), we describe the spectrum of the incident IUV radiation from stars by a power law with an index α:

$$I_{IUV}(\nu) = I_0(\nu_{HI})\left(\frac{\nu}{\nu_{HI}}\right)^{-\alpha}, \tag{14}$$

where ν is the frequency of photons and $I_0(\nu_{HI})$ is the intensity at the ionization frequency of neutral hydrogen ($\nu_{HI} = 3.3 \times 10^{15}$ Hz). We use the same spectrum to estimate Γ_n ($n = 13$, 14, 15) by extending the spectrum down to 1.8×10^{14} Hz corresponding to the photon energy ($h\nu$) of 0.74 eV. This corresponds to the threshold energy for the photoionization of H^- (Table 2). $I_{IUV}(\nu)$ could be obtained from a synthetic spectrum of stellar populations, but in this paper we simply set $\alpha = 5$ for the following two reasons: (i) The spectral shape is uncertain because of the interstellar dust extinction. In particular, little is known about the extinction curve in an extremely metal-poor environment. (ii) Even in the case of $\alpha = 5$, where the largest number of H_2 dissociating photons are produced among the four spectra examined in Kitayama et al. (2001), dissociation of H_2 is negligible in the presence of dust grains. The normalization of the intensity is determined from

$$\frac{L_{UV,0}\exp(-\tau_{disc})}{4\pi r_{disc}^2} = \int_{\nu_{min}}^{\infty} I_{IUV}(\nu)\,d\nu, \tag{15}$$

where we define ν_{min} as the minimum frequency where OB stars dominate the radiative energy of star-forming galaxies ($\simeq 10^{15}$ Hz), $L_{UV,0}$ is the UV luminosity estimated in equation (28), and τ_{disc} is the typical dust optical depth in the disc. This typical optical depth can be simply estimated by multiplying the typical column density of dust in the direction of the disc plane, $n_{dust}r_{dust}$, by the absorption cross-section of dust against UV light, $\pi a^2 Q_{UV}$, as

$$\tau_{disc} = \pi a^2 n_{dust} r_{disc}, \tag{16}$$

where a is the grain radius (spherical grains are assumed). The method for estimating $L_{UV,0}$ and n_{dust} will be described later in Section 2.5.1.

The H_2 photodissociation cross-section is estimated from the rate given by Abel et al. (1997). However, if the column density of H_2 becomes larger than 10^{14} cm^{-2}, self-shielding effects become important (Draine & Bertoldi 1996). Therefore, we use the following expression for the H_2 dissociation rate:

$$\Gamma_{13} = (4\pi)1.1 \times 10^8\, I_{IUV}(3.1 \times 10^{15}\,\mathrm{Hz})\left(\frac{n_H f_{H_2} r_{disc}}{10^{14}\,\mathrm{cm}^{-2}}\right)^{-0.75} \mathrm{s}^{-1}, \tag{17}$$

where I_{IUV} is in cgs units.

For the H_2 formation on grains, recent experimental results have indicated that $S \sim 0$ (the sticking efficiency of hydrogen atoms; Appendix A) for $T_{dust} > 20$ K (Katz et al. 1999). Such a low-temperature threshold for H_2 formation suggests the following scenario. Because of the thermal coupling between the dust and the cosmic microwave background (CMB) of temperature $T_{CMB} = 2.7(1 + z)$ K, molecular formation on grains might have been strongly suppressed when $T_{CMB} \gtrsim 20$ K or $z \gtrsim 7$. As a result, galaxies start to form stars actively when $z \sim 7$. In this case, $z \sim 7$ is the typical redshift for the onset of active star formation. Since such a typical redshift, if it exists, could be in principle detected as an enhancement of galaxy number counts at a certain flux level, it is worth considering such a typical 'formation epoch' in this paper. We reconsider this point in detail in Section 4.

SNII affect the abundance of H_2 as they create regions filled with hot gas ($T \sim 10^6$ K). In such an environment H_2 is destroyed, but it re-forms after the gas cools; this predominantly occurs in cooled shells (Shapiro & Kang 1987; Ferrara 1998; we note that our f_{H_2} is roughly twice that of Shapiro & Kang) and f_{H_2} becomes a few $\times 10^{-3}$. We cannot consider these effects in this paper, because our model, which only treats averaged quantities over the whole galaxy, cannot describe local bubbles and shells produced by SNII. We expect that the formation of H_2 on dust surfaces and in the cold shells keeps f_{H_2} from decreasing significantly.

In order to calculate the temperature evolution, cooling and heating should be included in our model. We adopt the cooling functions summarized in section 2.3 of Hutchings et al. (2002), i.e. cooling by molecular hydrogen, and collisional excitation and ionization of atomic hydrogen. Again cooling by helium is neglected because Hutchings et al. (2002) have shown that the temperature evolution is little affected by the helium cooling. For the heating by stellar IUV radiation, we adopt equation (A21) of Kitayama & Ikeuchi (2000). The initial value for T_{gas} is assumed to be T_{vir}.

2.2 Star formation law

The adopted star formation law is central to this paper, because we propose a new 'paradigm' based on the fact that the stars are formed during the final cooling by molecular hydrogen. If the molecular gas is abundant, stars are formed as a result of a dynamical collapse of gas. Since a representative time-scale of the dynamics of the gas disc is the circular time-scale, t_{cir}, we expect that the star formation rate ψ is roughly M_{gas}/t_{cir} in a fully molecular gas. Most of the 'semi-analytic' recipes of galaxy evolution (e.g. Kauffmann & Charlot 1998; Somerville & Primack 1999; Cole et al. 2000; Granato et al. 2000; Nagashima et al. 2001; cf. White & Frenk 1991) assume this kind of law (the dependence on the circular velocity is non-linear though). However, since the final coolant is molecular hydrogen, we should include the hydrogen content in the formulation to obtain a more physical star formation law. Therefore, we assume the following form for the star formation rate:

$$\psi(t) = f_{H_2}(t) M_{gas}/t_{cir}, \tag{18}$$

where M_{gas} and t_{cir} are taken to be constant in time.

Although the following results are critically dependent on the assumed form of f_{H_2}, the experimental evidence shows that star formation depends positively on molecular abundance (e.g. Rana & Wilkinson 1986; Wilson et al. 2000; Walter et al. 2002; but see e.g. Buat, Deharveng & Donas 1989; Tosi & Diaz 1990). Equation (18) is given 'as a first approximation' in this paper to include this experimentally supported law. Although multiphase behavior of the ISM can also be important (McKee & Ostriker 1977; Ikeuchi 1988;

Norman & Spaans 1996), this equation is expected to approximate the star formation rate of the whole galaxy in the framework of our one-zone treatment.

We are interested in objects whose virial temperature is typically larger than 10^4 K (Section 2.1). Madau et al. (2001) have argued that such objects cool on a time-scale much shorter than the dynamical time-scale and consequently experience an initial strong episode of star formation. Our approach in this paper is conservative in the sense that active star formation does not occur until a significant amount of hydrogen molecules is produced. However, even in our 'conservative' treatment, a burst of star formation occurs as a result of molecular formation on dust grains (Section 3). Therefore, a scenario similar to, albeit physically different from, those of Ciardi et al. (2000), Madau et al. (2001) and Barkana (2002) emerges from the present study.

2.3 Evolution of dust content

Because of the short cosmic time-scale between $z=5$ and 20 ($\lesssim$1 Gyr), the contribution of Type Ia supernovae (SNIa) and winds from late-type stars to dust formation is assumed to be negligible. In this case, SNII are the dominant sources for dust formation. The rate of SNII as a function of time, $\gamma(t)$, is given by

$$\gamma(t) = \int_{8\,\mathrm{M}_\odot}^{\infty} \psi(t-\tau_m)\phi(m)\,\mathrm{d}m, \tag{19}$$

where $\psi(t)$ is the star formation rate (SFR) at t (for $t<0$, $\psi(t)=0$), $\phi(m)$ is the initial mass function (IMF) [the definition of the IMF is the same as that in Tinsley (1980)], τ_m is the lifetime of a star whose mass is m, and we assumed that stars with $m>8\,\mathrm{M}_\odot$ produce SNII. In this paper, we assume a Salpeter IMF [$\phi(m)\propto m^{-2.35}$] with the stellar mass range of 0.1–60 $\mathrm{M}_\odot$. It has been suggested that the IMF is much more weighted to massive stars, i.e. top-heavy, in primeval galaxies (e.g. Bromm et al. 2002). In a top-heavy environment, the production of dust by massive stars is enhanced. As a result, dust amount, and thus molecular amount, in galaxies would be larger than that predicted in this paper. Here, we 'conservatively' assume the Salpeter IMF.

Dust destruction by SNII can be important. The destruction time-scale τ_{SN} is estimated to be (McKee 1989; Lisenfeld & Ferrara 1998)

$$\tau_{\mathrm{SN}} = \frac{M_{\mathrm{g}}}{\gamma\epsilon M_{\mathrm{s}}(100\,\mathrm{km\,s^{-1}})}, \tag{20}$$

where $M_{\mathrm{s}}(100\,\mathrm{km\,s^{-1}})=6.8\times10^3\,\mathrm{M}_\odot$ (Lisenfeld & Ferrara 1998) is the mass accelerated to 100 km s^{-1} by a SN blast, γ is the SNII rate, and $\epsilon\sim0.1$ (McKee 1989) is the efficiency of dust destruction in a medium shocked by a SNII. Since we are interested in the first star formation activity, we assume the relation between stellar mass and lifetime of zero-metallicity stars in table 6 of Schaerer (2002) (the case without mass loss is applied).

Then the rate of increase of M_{d} is written as

$$\frac{\mathrm{d}M_{\mathrm{d}}}{\mathrm{d}t} = m_{\mathrm{d}}\gamma - \frac{M_{\mathrm{d}}}{\tau_{\mathrm{SN}}}, \tag{21}$$

where m_{d} is the typical dust mass produced in a SNII. Todini & Ferrara (2001) showed that m_{d} varies with progenitor mass and metallicity. There is also some uncertainty in the explosion energy of a SNII. The Salpeter IMF-weighted mean of dust mass produced per SNII for (1) $Z=0$, case A, (2) $Z=0$, case B, (3) $Z=10^{-2}\,\mathrm{Z}_\odot$, case A, and (4) $Z=10^{-2}\,\mathrm{Z}_\odot$, case B, are: (1) 0.22, (2) 0.46, (3) 0.45 and (4) 0.63 $\mathrm{M}_\odot$, respectively (here Z is the metallicity, and cases A and B correspond to low and high explosion energy,[5] respectively). We adopt the average of the four cases, i.e. $m_{\mathrm{d}}\simeq0.4\,\mathrm{M}_\odot$ but we should remember that m_{d} can have a range (from 0.22 to 0.63 $\mathrm{M}_\odot$). Since dust destruction is negligible, as shown later, our final value of the dust mass is approximately proportional to the adopted one for m_{d}.

2.4 Evolution of metal content

The evolution of metal content can be predicted once the star formation history and metal yield per SNII are fixed (e.g. Tinsley 1980). Suginohara, Suginohara & Spergel (1999) have proposed that the fluctuations in space and wavelength of (sub)millimetre background radiation made of high-redshift metal lines can be used as an indicator of structure formation at high redshift. Here we obtain the metal mass injected in the gas phase by subtracting the dust mass from the metal mass. The evolution of the mass of a heavy element (species i) in the gas phase of a galaxy, M_i, is thus calculated by

$$\frac{\mathrm{d}m_i}{\mathrm{d}t} = m_i\gamma - \frac{\mathrm{d}m_{\mathrm{dust},i}}{\mathrm{d}t}, \tag{22}$$

where m_i is the averaged mass of element i formed per SNII and $M_{\mathrm{dust},i}$ is the mass of element i in the dust phase. According to the calculation of Todini & Ferrara (2001), dust contains 15 per cent of oxygen and 36 per cent of carbon. Therefore, we assume that $M_{\mathrm{dust,O}}=0.15M_{\mathrm{dust}}$ and $M_{\mathrm{dust,C}}=0.36M_{\mathrm{dust}}$ (we take the same average as that in Section 2.3). In Table 4 (see later), we list m_i for carbon and oxygen. When calculating m_i, we adopted the results by Woosley & Weaver (1995) and took the same mean as that in Section 2.3. Suginohara et al. (1999) also considered nitrogen, but we have not included this species, as the production of nitrogen in an SNII is one or two orders of magnitude less than that of oxygen or carbon.

2.5 Radiative properties

2.5.1 UV and FIR

Probably the most direct way to reveal high-redshift dust is to observe FIR emission. We now derive the evolution of galactic FIR luminosity and dust temperature. Because of the large cross-section of dust against IUV light and the intense IUV radiation field in a star-forming galaxy, we can assume that the FIR luminosity is equal to the absorbed energy of IUV light.

First, we should estimate the fraction of the IUV radiation absorbed by dust. For the convenience of the following calculation, we define the following typical optical depth in the vertical direction of the disc, τ_0, as

$$\tau_0 \equiv \pi a^2 Q_{\mathrm{UV}} n_{\mathrm{dust}} H. \tag{23}$$

In this paper we assume a single value for a, because there is a typical size of dust produced by SNII as shown by Todini & Ferrara (2001). We note that this optical depth is different from τ_{dust} in equation (15), where we needed an optical depth in the disc direction. Here, the optical depth in the vertical direction is useful as we see in the following.

Since τ_0 is independent of H, the optical depth of the dust does not depend on the treatment of r_{disc}/H in Section 2.1.1. The dust density is related to the mean dust number density as

$$\tfrac{4}{3}\pi a^3\delta n_{\mathrm{dust}}\pi r_{\mathrm{disc}}^2 2H = M_{\mathrm{dust}}, \tag{24}$$

[5] The kinetic energies given to the ejecta are $\sim1.2\times10^{51}$ and $\sim2\times10^{51}$ erg s for cases A and B, respectively.

where δ is the grain material density. By solving equation (24) for $n_{\rm dust}$ and substituting it into equation (23), we obtain

$$\tau_0 = \frac{3}{8\pi}\frac{Q_{\rm UV} M_{\rm d}}{a\delta r_{\rm disc}^2}. \tag{25}$$

If the angle between the direction of IUV light propagation and the vertical direction of the disc is θ, the intensity of the light becomes roughly $\exp(-\tau_0/\cos\theta)$. Therefore, the luminosity of IUV light escaping from the galactic disc, $L_{\rm UV}$, is estimated to be

$$L_{\rm UV} \simeq L_{\rm UV,0}\left\langle \exp\left(-\frac{\tau_0}{\cos\theta}\right)\right\rangle_\theta = L_{\rm UV,0}\, E_2(\tau_0), \tag{26}$$

where $\langle\ \rangle_\theta$ indicates the mean over the solid angle and $L_{\rm UV,0}$ is the intrinsic UV luminosity of the galaxy. The exponential integral $E_n(x)$ ($n = 0, 1, 2, \ldots; x > 0$) is defined as

$$E_n(x) \equiv x^{n-1}\int_x^\infty \frac{\exp(-y)}{y}\,{\rm d}y. \tag{27}$$

$L_{\rm UV,0}$ is assumed to be equal to the total luminosity of OB stars whose mass is larger than 3 $M_\odot$ (Cox 2000):

$$L_{\rm UV,0}(t) = \int_{3M_\odot}^\infty {\rm d}m \int_0^{\tau_m} {\rm d}t'\, L(m)\phi(m)\psi(t-t'), \tag{28}$$

where $L(m)$ is the stellar luminosity as a function of stellar mass (m). For $L(m)$, we adopt the model of zero-metallicity stars without mass loss in Schaerer (2002). We fix this relation as a first approximation in this paper.

We adopt $a \simeq 0.03$ μm (Todini & Ferrara 2001), $Q_{\rm UV} \simeq 1$ and $\delta \simeq 2$ g cm^{-3} (Draine & Lee 1984). We only consider a single value of a, because there is a well-defined sharp peak in the dust size distribution by Todini & Ferrara (2001). Then we obtain the energy absorbed by dust. We assume that all the absorbed energy is re-emitted in the FIR. Thus, the FIR luminosity $L_{\rm FIR}$ becomes

$$L_{\rm FIR} = L_{\rm UV,0} - L_{\rm UV}. \tag{29}$$

The dust temperature $T_{\rm dust}$ is determined from the equation derived by Hirashita et al. (2002a) based on the dust emissivity given by Draine & Lee (1984) for $a = 0.03$ μm:

$$T_{\rm d} = 20\left(\frac{L_{\rm FIR}/{\rm L}_\odot}{2.5\times10^2\, M_{\rm d}/{\rm M}_\odot}\right)^{1/6}{\rm K}. \tag{30}$$

2.5.2 *Metal lines*

We next calculate the luminosities of the metal lines. Our model calculation indicates that almost all the gas is in neutral form ($x \ll 1$ and $f_{\rm H_2} \ll 1$); hence we consider lines typical for neutral regions. The most interesting lines are listed in Table 4 (see later). For spontaneous transition from an upper level 'u' to a lower level 'ℓ', the total luminosity of the line with frequency $\nu_{\rm line}$ (line = C609, C370, O63, O146 for C I 609 μm, C I 370 μm, O I 63.2 μm and O I 146 μm, respectively) becomes

$$L_{\rm line} = h_{\rm P}\nu_{\rm line}\mathcal{N}_{\rm u}A_{{\rm u}\ell}, \tag{31}$$

where $h_{\rm P}$ is the Planck constant, $\mathcal{N}_{\rm u}$ is the total number of atoms in the upper level in the whole galaxy, and $A_{{\rm u}\ell}$ is the Einstein coefficient of the spontaneous emission. We assume that all the carbon and oxygen are neutral; we will also consider the C II 158 μm line, which is also emitted from the neutral medium (Tielens & Hollenbach 1985; Liszt 2002). If the time-scale of the spontaneous emission is longer than that of the collisional excitation, the fraction within the state is proportional to $2g+1$ (i.e. 1/9, 3/9 and 5/9 for $^3{\rm P}_0$, $^3{\rm P}_1$ and $^3{\rm P}_2$, respectively). However, if the density is so low that collisional excitation does not occur as frequently as spontaneous emission, the population in the upper level is reduced. We include this effect of low density by multiplying the factor $\mathcal{F}$ described in Appendix B.

The line intensity is estimated for the case where the population ratio is determined by $2g+1$. Since this gives us the maximum line intensity, we denote the intensity as $L_{\rm line}^{\rm max}$; more realistically, the line intensity is closer to $\mathcal{F}L_{\rm line}^{\rm max}$. We estimate $\mathcal{N}_{\rm u}$ from the metal mass in equation (22) and the number fraction in the upper level. The actual intensity of metal line is reduced by a factor $\mathcal{F}$. However, a precise determination of $\mathcal{F}$ requires a detailed treatment of the evolution of gas density. As discussed in Section 2.1.1, our present framework can only provide a first-order estimate of such a quantity; therefore, only $L_{\rm line}^{\rm max}$ is calculated in this paper. Nevertheless we propose a simple method to estimate $\mathcal{F}$ in Appendix B. When we calculate the C II 158 μm line intensity, we assume that all the carbon atoms are in the form of C^+.

3 RESULTS FOR FIDUCIAL GALAXIES

3.1 A typical primeval galaxy

In the following we show the evolution of some characteristic quantities predicted by our model for a galaxy with $(M_{\rm vir}, z_{\rm vir}) = (10^9\,{\rm M}_\odot, 10)$, corresponding to a 2.5σ density fluctuation of the cosmological density field. The qualitative behaviour of the quantities are similar for other objects of interest to the present study. In the next subsection, we explore various $(M_{\rm vir}, z_{\rm vir})$ values.

Using the equations above, we simultaneously calculate the time evolution of $f_{\rm H_2}$, ψ, $M_{\rm dust}$ and various kinds of luminosities in a self-consistent manner. In Fig. 1, we show the evolution of the molecular fraction $f_{\rm H_2}$ (solid line of Fig. 1a), and the star formation rate ψ (solid line of Fig. 1b) for an object $z_{\rm vir} = 10$ and $M_{\rm vir} = 10^9\,{\rm M}_\odot$. We show the results up to $10t_{\rm cir}$ ($\simeq 7.8\times10^8$ yr), which is comparable to the time between $z = 10$ and $z = 5$. At $t = 10t_{\rm cir}$, ∼30 per cent of the gas is converted into stars. Therefore, the calculation further than this time is not consistent with our assumptions, which neglect the gas conversion into stars. The gas temperature rapidly drops and reaches $\lesssim$300 K within 10^7 yr.

For other sets of $(M_{\rm vir}, z_{\rm vir})$, an enhancement of the star formation at 3–5$t_{\rm cir}$ is commonly seen. This results from the H_2 formation on dust grains. The dotted lines of Figs 1(a) and (b) indicate the case in which we neglect the dust (i.e. $M_{\rm d} = 0$) at all times. In this case, after stars form, $f_{\rm H_2}$ decreases because of photodissociation. Comparing the solid and dotted lines in Figs 1(a) and (b), we conclude that the existence of dust is essential in causing a strong star formation activity in primeval galaxies.

In Fig. 2, we show the evolution of dust, oxygen and carbon (solid, dotted and dashed lines, respectively). The mass fraction relative to the total gas mass is also shown on the right-hand axis. Note that the solar abundances for oxygen and carbon are 1.0×10^{-2} and 3.4×10^{-3} in mass ratio, respectively (Anders & Grevesse 1989; Cox 2000). We see rapid rises of those masses around $t \sim 4t_{\rm cir}$ (marked with the vertical dashed line). We also show the case in which dust destruction by SNII is neglected (dot-dashed line): dust destruction has little influence on the dust amount during the early ($\lesssim$ several $t_{\rm cir}$) evolution.

In Fig. 3, we show the evolution of three luminosities: $L_{\rm UV}$, $L_{\rm FIR}$ and $L_{\rm O146}^{\rm max}$ (solid, dotted and dot-dashed lines, respectively). Whereas $L_{\rm FIR}$ and $L_{\rm O146}^{\rm max}$ grow rapidly around $t \sim 4t_{\rm cir}$, $L_{\rm UV}$ does not increase

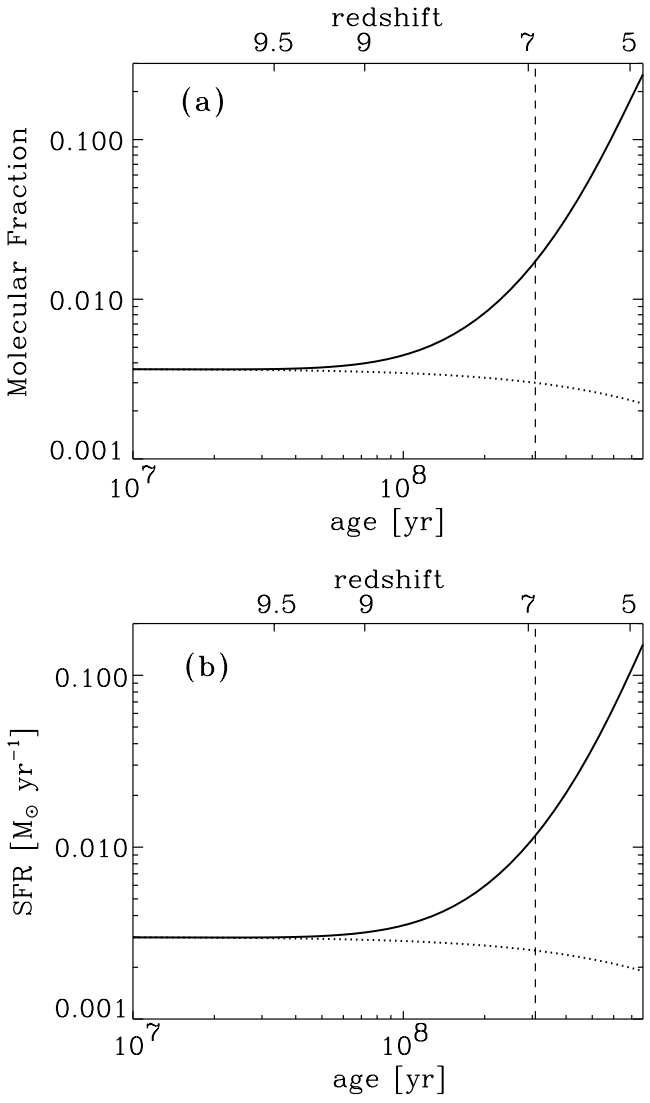

Figure 1. Time evolution of (a) the molecular fraction and (b) the star formation rate for a galaxy with $z_{\rm vir} = 10$ and $M_{\rm vir} = 10^9$ M$_\odot$ corresponding to the 2.5σ density fluctuation. The evolution in the first 10 circular times is shown. The solid line is for the case where we consider dust (and therefore H_2 formation on grains), and the dotted line is for the case of no dust production ($M_{\rm dust} = 0$). The vertical dashed line marks the four circular time-scales, where the typical quantities are defined in the text and in Table 3. On the top axis, we show the corresponding redshifts.

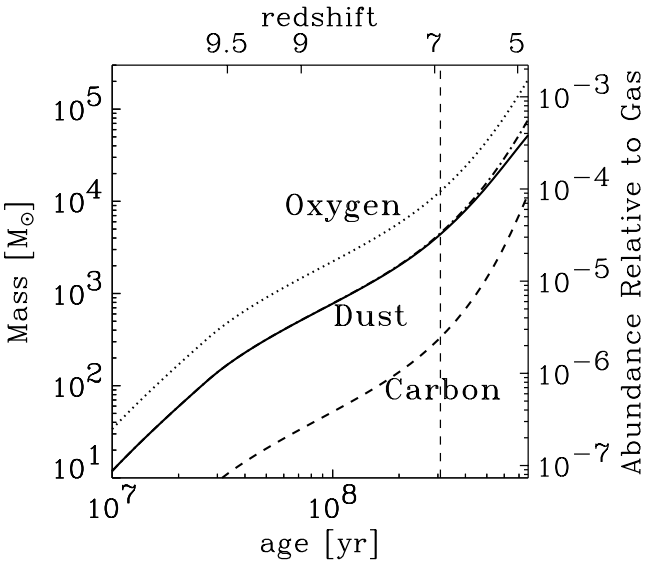

Figure 2. Time evolution of the masses of dust, oxygen (in gas phase) and carbon (in gas phase) in the same galaxy as Fig. 1 (solid, dotted and dashed lines, respectively). The dot-dashed line represents the case in which dust destruction is neglected. The vertical dashed line shows the four circular time-scales.

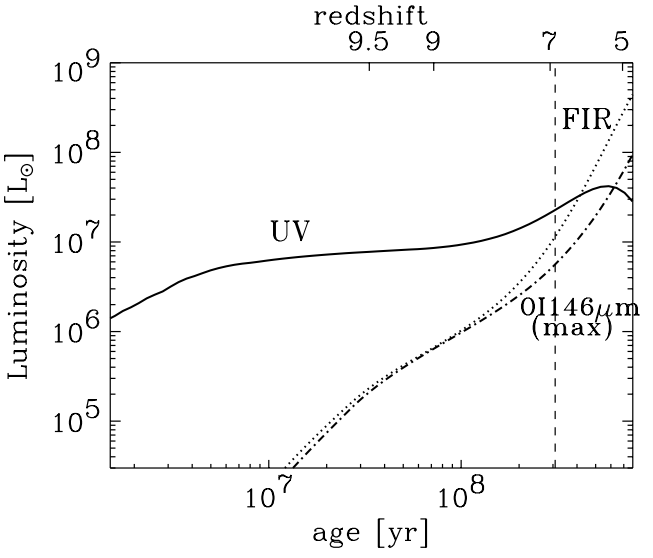

Figure 3. Time evolution of the ultraviolet luminosity (solid line), the far-infrared luminosity (dotted line) and the maximum line luminosity of O I 146 μm ($L_{\rm O146}^{\rm max}$) (dot-dashed line) for the same galaxy as in Fig. 1. The vertical dashed line shows the four circular time-scales.

as significantly as the other two luminosities because of dust extinction. The FIR luminosity becomes comparable to the UV luminosity soon after the active star formation phase starts. Therefore, even in the early stages of star formation, dust absorbs a significant fraction of stellar light and reprocesses it to the FIR range. This is because of the dense and compact nature of high-redshift galaxies [$r_{\rm vir} \propto (1+z)^{-1}$ with a fixed $M_{\rm vir}$]. Therefore, even at early cosmic epochs ($z > 5$) simultaneous observations of FIR emission from dust and of the UV/NIR stellar light is crucial to trace the total radiative energy from galaxies.

3.2 Dependence on ($M_{\rm vir}$, $z_{\rm vir}$)

Table 3 clarifies the dependence of various quantities on $M_{\rm vir}$ and $z_{\rm vir}$. We define the typical star formation rate for each object, $\bar{\psi}(M_{\rm vir}, z_{\rm vir})$, as $\psi(4t_{\rm cir})$. This is because after four circular times objects have consumed ∼5 per cent of the gas. Since it is empirically known that the star formation efficiency during an episode of star formation activity is $\lesssim$10 per cent (e.g. Inoue, Hirashita & Kamaya 2000; Barkana 2002), the definition yields a good working value. Moreover, the value at $t = 4t_{\rm cir}$ gives a good average for the star formation rates over the Hubble time-scale at $z_{\rm vir}$ within a factor of ∼2. In Table 3, we show the typical star formation rate as a function of $z_{\rm vir}$ and $M_{\rm vir}$. In Table 3 we also show other quantities, all of which are estimated at $t = 4t_{\rm cir}$ (i.e. the quantities with the overbars indicate the typical quantities estimated at $t = 4t_{\rm cir}$).

Table 3. Typical quantities for various sets of ($M_{\rm vir}$, $z_{\rm vir}$).

$M_{\rm vir}$ ($M_\odot$)	$\bar{\psi}$ ($M_\odot$ yr^{-1})	$\bar{L}_{\rm FIR}$ ($L_\odot$)	$\bar{L}_{\rm UV}$ ($L_\odot$)	$\bar{L}^{\rm max}_{\rm C609}$ ($L_\odot$)	$\bar{L}^{\rm max}_{\rm C370}$ ($L_\odot$)	$\bar{L}^{\rm max}_{\rm O63}$ ($L_\odot$)	$\bar{L}^{\rm max}_{\rm O146}$ ($L_\odot$)	$\bar{L}^{\rm max}_{\rm C158}$ ($L_\odot$)	$\bar{T}_{\rm dust}$ (K)
				$z_{\rm vir} = 20$					
10^8	2.5e−3	2.5e6	4.0e6	4.9e2	5.3e1	1.7e7	4.2e5	6.1e3	44
10^9	1.9e−1	4.0e8	4.6e7	2.1e4	2.2e3	6.1e8	1.5e7	2.6e5	57
10^{10}	4.4e0	1.0e10	1.4e7	4.5e5	4.9e4	1.1e10	2.7e8	5.6e6	61
10^{11}	4.3e1	9.8e10	4.2e5	4.3e6	4.7e5	1.1e11	2.7e9	5.4e7	61
				$z_{\rm vir} = 15$					
10^8	9.5e−4	6.7e5	2.1e6	4.0e2	4.3e1	1.4e7	3.5e5	5.0e3	37
10^9	7.3e−2	1.4e8	5.1e7	1.8e4	1.9e3	5.2e8	1.3e7	2.2e5	49
10^{10}	2.7e0	6.8e9	5.2e7	5.9e5	6.4e4	1.4e10	3.3e8	7.3e6	55
10^{11}	2.4e1	6.0e10	1.5e7	4.9e6	5.3e5	1.2e11	2.9e9	6.0e7	55
				$z_{\rm vir} = 12$					
10^8	4.0e−4	1.7e5	1.0e6	2.8e2	3.0e1	1.0e7	2.5e5	3.5e3	31
10^9	2.7e−2	3.8e7	3.7e7	1.0e4	1.1e3	3.4e8	8.2e6	1.3e5	42
10^{10}	1.3e0	3.3e9	2.0e8	4.2e5	4.5e4	1.1e10	2.6e8	5.2e6	51
10^{11}	1.2e1	3.0e10	2.5e8	3.5e6	3.7e5	9.1e10	2.2e9	4.3e7	51
				$z_{\rm vir} = 9$					
10^8	1.4e−4	3.1e4	4.2e5	1.8e2	1.9e1	6.5e6	1.6e5	2.2e3	25
10^9	7.9e−3	6.5e6	1.7e7	5.9e3	6.3e2	2.0e8	4.9e6	7.2e4	34
10^{10}	5.3e−1	1.2e9	3.3e8	2.8e5	3.0e4	7.6e9	1.8e8	3.4e6	45
10^{11}	4.6e0	1.2e10	1.1e9	2.3e6	2.5e5	6.5e10	1.6e9	2.8e7	46
				$z_{\rm vir} = 6$					
10^8	4.1e−5	3.4e3	1.3e5	1.0e2	1.1e1	3.9e6	9.5e4	1.3e3	19
10^9	1.8e−3	5.9e5	4.9e6	3.0e3	3.3e2	1.1e8	2.7e6	3.8e4	25
10^{10}	1.3e−1	1.7e8	2.2e8	1.4e5	1.5e4	4.2e9	1.0e8	1.7e6	36
10^{11}	1.4e0	2.8e9	1.5e9	1.4e6	1.5e5	4.3e10	1.1e9	1.7e7	39

All quantities except for $\bar{L}_{\rm UV}$ are monotonically increasing functions of both $M_{\rm vir}$ and $z_{\rm vir}$. An object with larger $M_{\rm vir}$ tends to contain a larger gas mass ($M_{\rm gas}$). An object with larger $z_{\rm vir}$ tends to have a short $t_{\rm cir}$ [$\propto (1+z_{\rm vir})^{-1.5}$] because of a small $r_{\rm disc} \propto (1+z_{\rm vir})^{-1}$ and a large $v_{\rm c} \propto (1+z_{\rm vir})^{0.5}$. Therefore, the star formation law (equation 18) indicates that $\bar{\psi}$ becomes an increasing function of both $M_{\rm vir}$ and $z_{\rm vir}$. The larger the star formation rate, the larger are the metal production, the dust production and the intrinsic OB star luminosity. As a result, almost all quantities become increasing functions of both $M_{\rm vir}$ and $z_{\rm vir}$. On the contrary, $\bar{L}_{\rm UV}$ is not monotonic. For objects with $z_{\rm vir} \gtrsim 15$ and $M_{\rm vir} \gtrsim 10^{10}\,{\rm M}_\odot$, $\bar{L}_{\rm UV}$ decreases as $M_{\rm vir}$ and $z_{\rm vir}$ increase. This is because of the compactness of high-redshift objects. Dust accumulation in a compact region makes the optical depth of dust very large; hence UV radiation is efficiently absorbed by dust. However, objects with $z_{\rm vir} \gtrsim 15$ and $M_{\rm vir} \gtrsim 10^{10}\,{\rm M}_\odot$ are extremely rare because they correspond to density fluctuations $\gtrsim 4\sigma$.

The temperature of dust is generally higher than that observed in normal spiral galaxies (∼20 K), because the compactness (meaning high density) of the high-redshift galaxies leads to a strong stellar radiation field. For a nearby dwarf galaxy, SBS 0335−052, the compactness of the star-forming region is also suggested to result in a high dust temperature (Dale et al. 2001; Hirashita et al. 2002a).

4 STATISTICAL PREDICTIONS

Future observations will provide large samples of galaxies at $z > 5$. Therefore, predictions of the statistical properties of galaxies in such a redshift range are very valuable. Using the result above, we focus on cosmic star formation rate (Tinsley & Danly 1980; Madau et al. 1996), number counts of galaxies and integrated light (Partridge & Peebles 1967), where 'integrated' means the sum of the contributions from all the galaxies of interest.

4.1 Cosmic star formation history

The star formation rate per unit comoving volume at the redshift z, $\Psi(z)$, is written as

$$\Psi(z) = \int_{M_{\rm min}}^{M_{\rm max}} {\rm d}M\, \psi(M,z) \frac{\partial n(M,z)}{\partial M}, \tag{32}$$

where $n(M,z)$ is the comoving number density of haloes with masses larger than M at z, and $\psi(M,z)$ is the star formation rate of an object with mass M at z.

In equation (32), $M_{\rm min}$ is set equal to the maximum mass of a galaxy whose gas is blown away by SNII in order to exclude objects that do not form stars continuously. From a fitting to the result of Ciardi et al. (2000), we adopt

$$M_{\rm min} = \frac{5\times 10^{10}}{(1+z)^{1.5}} {\rm M}_\odot. \tag{33}$$

Ciardi et al. presented three cases (A, B and C) for various cooled gas fraction, star formation efficiency and escaped photon fraction, all of which are inherent to their model. In equation (33), we adopt their fiducial case A. Even for the other cases, the following results are not changed at all, because galaxies whose mass is as low as $10^9\,{\rm M}_\odot$ do not contribute to the number counts at the flux level of interest. Ciardi et al.'s case A indicates that 1.2 per cent ($=f_{\rm b} f_\star$) of baryons are converted into stars in a dynamical time. This gives a star formation rate comparable to the one that we find at $t = 4t_{\rm cir}$.

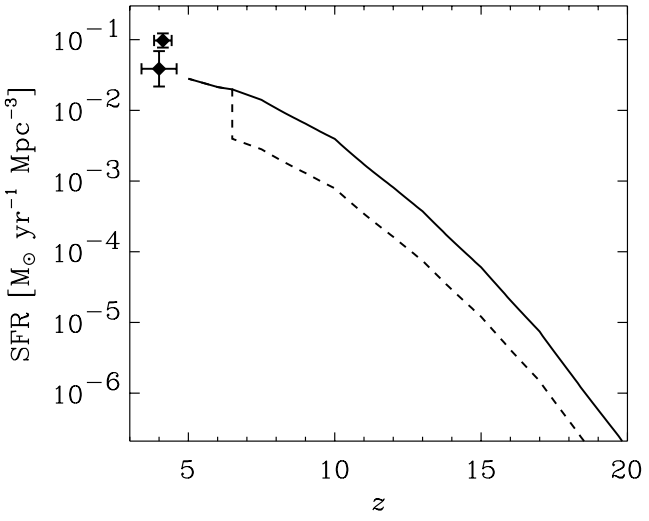

Figure 4. Star formation rate per unit comoving volume (solid line). The dotted line indicates the star formation history with a 'burst' (bSFH) at $z = 6.5$. The two data points around $z \sim 4$ are from Madau, Pozzetti & Dickinson (1998) (lower) and Steidel et al. (1999) (upper). These points have been corrected for the dust extinction by Steidel et al. (1999) and for the cosmological parameters chosen in this paper.

For the maximum mass we adopt $M_{\rm max} = 10^{13}\ {\rm M}_\odot$. As long as $M_{\rm max} \gtrsim 10^{13}\ {\rm M}_\odot$, the results are not changed at all, because the number of objects with $M_{\rm vir} > 10^{13}\ {\rm M}_\odot$ is negligible in all the considered redshift range ($5 < z < 20$). To derive $\partial n(M, z)/\partial M$, we use the Press–Schechter formalism (Press & Schechter 1974). We assume that the star formation rate is a function of the virial mass and the redshift as listed in Table 3; i.e. $\psi(M, z) = \bar{\psi}(M_{\rm vir} = M, z_{\rm vir} = z)$.

In Fig. 4, we show $\Psi(z)$ (solid line). The considered range of redshift is between $z_{\rm min} = 5$ and $z_{\rm max} = 20$, because we are interested in the first cosmic Gyr ($\sim$ Hubble time-scale at $z = 5$) and the number of galaxies with $z_{\rm max} > 20$ is negligible. The comoving stellar mass density formed by $z = 10$, 7 and 5 are 2.2×10^5, 2.7×10^6 and $1.3 \times 10^7\ {\rm M}_\odot\ {\rm Mpc}^{-3}$, respectively. In units of the critical density, these numbers correspond to $\Omega_\star = 1.6 \times 10^{-6}$, 2.0×10^{-5} and 9.6×10^{-5}, respectively.

As stated in Section 2.1.2, the suppression of H_2 formation on grains for $T_{\rm dust} \gtrsim 20$ K as shown experimentally by Katz et al. (1999) will introduce a characteristic star formation epoch ($z_{\rm burst}$). Their results indicate that H_2 formation on grains is allowed after the CMB temperature, $T_{\rm CMB}$, drops to $\lesssim$20 K ($z \lesssim 7$). Since the H_2 formation on dust is crucial to activate star formation in a galaxy, galaxies start to form stars actively at $z_{\rm burst} \sim 7$ in this scenario. Motivated by this, we have also investigated another star formation history activated at $z \sim z_{\rm burst}$. We call such a star formation history 'bursting star formation history' (bSFH). On the other hand, we call the star formation history without $z_{\rm burst}$ 'continuous SFH' (cSFH; the solid line of Fig. 4). Unless otherwise stated, we show the results for the cSFH.

Galaxies with an active star formation are found up to $z \sim 6.5$ (e.g. Hu et al. 2002). Moreover, Shanks et al. (2001) have shown that the space density of bright galaxies at $z \sim 6$ is comparable to the local space density (see also Ouchi et al. 2002), which suggests that the formation epoch of galaxies lies at $z > 6.5$. In this paper, we adopt the lower limit $z_{\rm burst} = 6.5$. As shown later, even for this low $z_{\rm burst}$ value, ALMA and *NGST* cannot clearly identify the existence of $z_{\rm burst}$. However, it is worth examining the typical flux level where the effect of $z_{\rm burst}$ on number counts is clearly seen.

Even in the presence of the typical burst redshift, $z_{\rm burst}$, the number of virialized galaxies does not change. The only difference is that star formation is largely suppressed for $z > z_{\rm burst}$ in the bSFH. Moreover, the star formation rate is typically enhanced by a factor of 5 at $4t_{\rm cir}$ as a result of the enhancement of molecular formation on accumulated dust. Therefore, for $\Psi(z)$ in the bSFH, we adopt a value equal to 1/5 of the one calculated in equation (32) if $z > z_{\rm burst}$. For $z < z_{\rm burst}$, we adopt the same value both for cSFH and for bSFH. The bSFH with $z_{\rm burst} = 6.5$ is shown by the dashed line in Fig. 4.

4.2 Galaxy number counts

We estimate the number of galaxies with observed flux greater than f_ν at an observed frequency ν by

$$N(>f_\nu, \nu) = \int_{z_{\rm min}}^{z_{\rm max}} {\rm d}z \int_{M_{\rm lim}(f_\nu, z)}^{M_{\rm max}} {\rm d}m \left[\frac{\partial n(M, z)}{\partial M} \frac{{\rm d}V(z)}{{\rm d}z} \right], \quad (34)$$

where $M_{\rm lim}(f_\nu, z)$ corresponds to the mass of the galaxy with specific luminosity L_ν, and

$$f_\nu = \frac{(1+z) L_{\nu(1+z)}}{4\pi d_{\rm L}^2}. \quad (35)$$

The luminosity distance, $d_{\rm L}$, is given by (Carroll, Press & Turner 1992)

$$d_{\rm L} = c(1+z) \int_0^z {\rm d}z' \, (1+z') \left| \frac{{\rm d}t}{{\rm d}z'} \right|, \quad (36)$$

where c is the light speed, and

$$\left| \frac{{\rm d}t}{{\rm d}z} \right|^{-1} = H_0 (1+z) \sqrt{(1+\Omega_{\rm M} z)(1+z)^2 - \Omega_\Lambda z (2+z)}. \quad (37)$$

The volume element per unit redshift, ${\rm d}V/{\rm d}z$, is written as

$$\frac{{\rm d}V(z)}{{\rm d}z} = \frac{4\pi c d_{\rm L}^2}{(1+z)} \left| \frac{{\rm d}t}{{\rm d}z} \right|. \quad (38)$$

We assume that L_ν depends on (M, z) and that L_ν increases monotonically with M for any z and any ν. The monotonicity is guaranteed in the submillimetre number counts, but not in the NIR counts. An NIR observation can detect the UV light in the rest frame of galaxies, and the UV luminosity is not a monotonically increasing function of $M_{\rm vir}$ for $z_{\rm vir} > 15$ (Table 3). Therefore, in calculating the NIR number counts, we set $z_{\rm max} = 15$. If $M_{\rm lim}(f_\nu, z) > M_{\rm max}$, we set $M_{\rm lim}(f_\nu)$ equal to $M_{\rm max}$.

Finally, we must fix L_ν as a function of M and z. We approximately identify (M, z) with $(M_{\rm vir}, z_{\rm vir})$, and use the quantities listed in Table 3 as a function of $(M_{\rm vir}, z_{\rm vir})$. The details of the calculation will be described separately in the following two subsections for submillimetre and NIR, respectively.

4.2.1 *Submillimetric bands*

We calculate the number counts due to continuum emission from dust. The peak of dust emission falls in the FIR range ($\sim$50–150 μm) in the rest frame of a galaxy. The peak of high-redshift ($z > 5$) galaxies is shifted to the submillimetre range in the observational rest frame. For example, for a galaxy at $z \sim 7$, observations around $\sim$800 μm should be performed. Here we consider three ALMA bands centred at 450, 850 and 1300 μm.

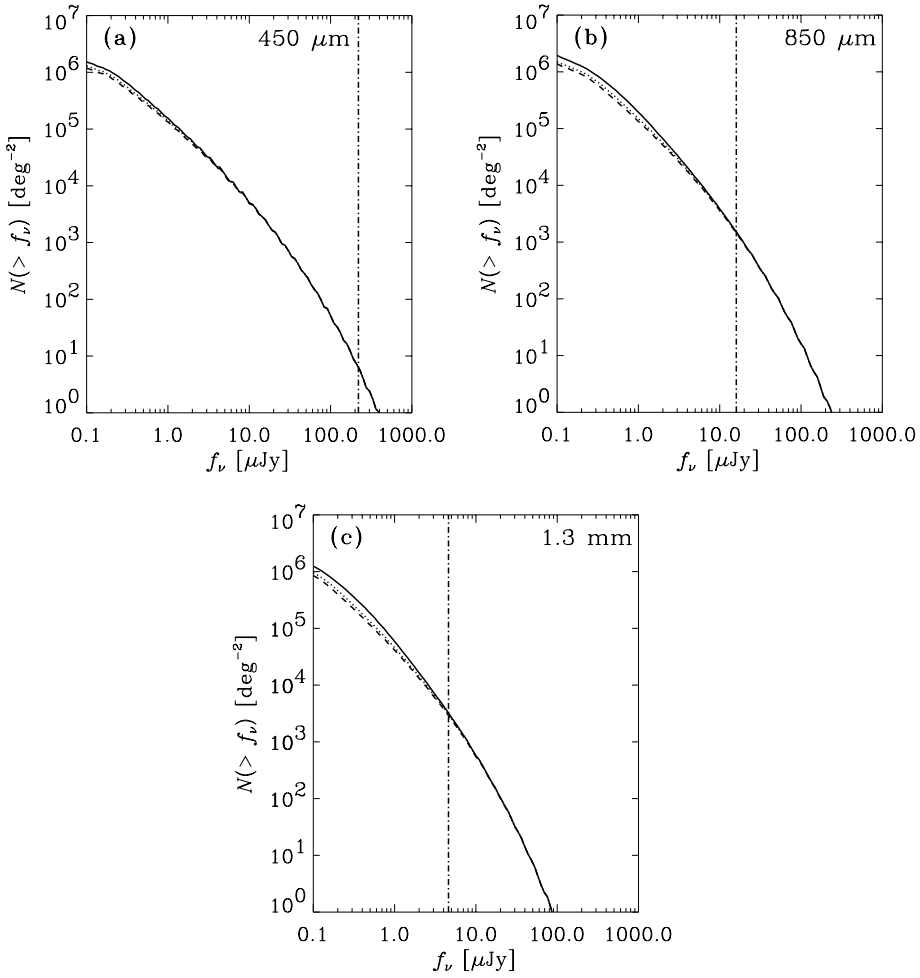

Figure 5. Theoretical predictions of the number counts of the high-redshift ($5 < z < 20$) galaxies in the ALMA bands (solid lines): (a) 450 μm, (b) 850 μm, and (c) 1.3 mm. The number counts of galaxies whose redshift range is $5 < z < 7$ are also shown (dotted lines). The dashed lines show the result for burst-mode star formation (bSFH), in which galaxies start to form stars actively at $z = 6.5$. The vertical dot-dashed lines show the ALMA detection limits.

The spectral energy distribution of the FIR emission from a galaxy is assumed to be a modified blackbody with a temperature $\bar{T}_{\rm dust}$ (listed in Table 3),

$$L_\nu = C\nu^2 B_\nu(\bar{T}_{\rm dust}), \tag{39}$$

where the coefficient C is determined so that the integration of L_ν for all the wavelength range becomes equal to $\bar{L}_{\rm FIR}(M_{\rm vir} = M, z_{\rm vir} = z)$.

From the above we can relate M and L_ν for each z using the relation between L_ν and ($\bar{L}_{\rm FIR}$, $\bar{T}_{\rm dust}$), and then equation (34) to obtain $N(f_\nu, \nu)$. In Figs 5(a)–(c), we show the number counts in three of the ALMA observational bands of 450, 850 and 1300 μm for galaxies with $5 < z < 20$ (solid lines) and with $5 < z < 7$ (dotted lines). The vertical lines show the detection limits, for which we adopt the same values as Takeuchi et al. (2001b) for the 5σ limits of 8-h integration (220, 16 and 4.6 μJy, respectively). We see that 5, 1.5×10^3 and 2.9×10^3 galaxies per square degree can be detected in the 450, 850 and 1300 μm bands, respectively. The high angular resolution of ALMA enables us to detect those galaxies without confusion. A bright source can make the detection of faint sources difficult because of a limited dynamic range of the detector. The probability that sources that are 10^3 (this number comes from the dynamic range of the detector of ALMA) times larger than the 5σ detection limit of ALMA exist in the field of view is negligible ($\lesssim 3 \times 10^{-4}$; Takeuchi et al. 2001b). From Fig. 5, it is also concluded that ALMA is sensitive to galaxies with $z \lesssim 7$.

4.2.2 *Near-infrared bands*

In order to test our theoretical prediction further, it is necessary to detect the stellar light, because dust production history is deeply related to star formation history. Since young galaxies are characterized by a strong UV stellar continuum produced by OB stars, we examine the detectability of the UV light, which is redshifted to the NIR range in our observational rest frame. For example, an observation at 1.8 μm can detect the stellar light at 3000 Å in the rest frame of a galaxy at $z = 5$, or that at 2000 Å at $z = 8$. In order to calculate the NIR number counts, we must fix the UV spectra. Although we have not included a spectral synthesis model of stellar populations [but we have used the stellar model by Schaerer (2002) in Section 2.5.1], the following constant spectral energy distribution can be used as a first approximation to the NIR number counts:

$$L_\nu(M, z) = \bar{L}_{\rm UV}(M_{\rm vir} = M, z_{\rm vir} = z)/\Delta\nu_{\rm UV}, \tag{40}$$

where $\Delta\nu_{\rm UV}$ is the typical width of the frequency range [$\sim$(1–8) $\times 10^{15}$ Hz; 400–3000 Å in wavelength] where OB stars dominate

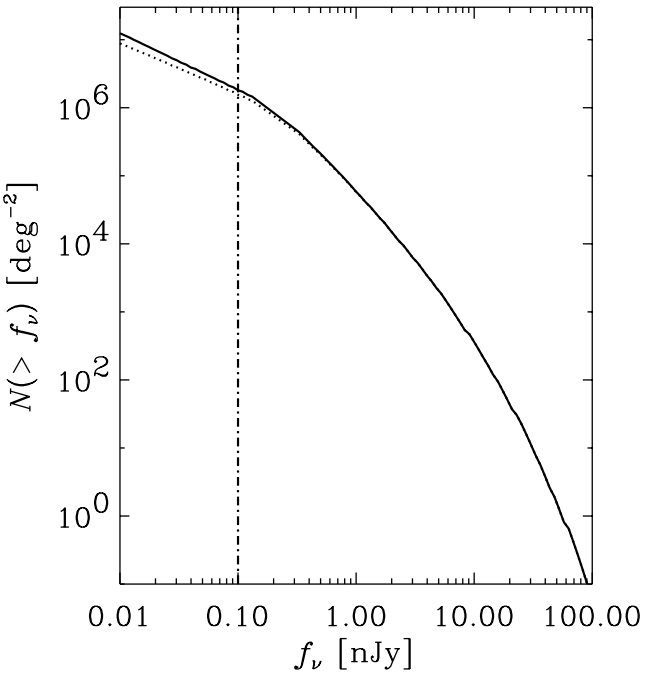

Figure 6. Number counts for high-redshift galaxies in the near-infrared. The solid and dotted lines show the number counts in the redshift range of $5 < z < 20$ and $5 < z < 7$, respectively. The vertical dot-dashed line indicates an expected detection limit (0.1 nJy) of the *NGST* photometry (Gardner & Satyapal 2000).

the luminosity. Here we assume $\Delta\nu_{\rm UV} = 7 \times 10^{15}$ Hz. We use the data listed in Table 3 for $\bar{L}_{\rm UV}$ as a function of $(M_{\rm vir}, z_{\rm vir})$.

In Fig. 6, we show the number counts in the NIR. The solid and dotted lines show the counts for $5 < z < 20$ and $5 < z < 7$, respectively. The vertical dot-dashed line shows a proposed detection limit of *NGST* at the NIR ($\simeq$0.1 nJy; Gardner & Satyapal 2000). We see that about 2×10^6 galaxies should be detected per square degree. The detection limit can be larger (1 nJy; Mather & Stockman 2000). In this case, about 10^5 galaxies are detected per square degree. These numbers are much larger than those derived for ALMA. In other words, all the ALMA sample for $z > 5$ is detected by *NGST*. Therefore, *NGST* can be used for the two aims: for an identification of ALMA sources, and for an exploration of the Universe deeper than ALMA. *NGST* can also detect galaxies whose redshift is larger than 7. The high-redshift $z > 5$ sample brighter than 0.1 nJy (1 nJy) contains 14 per cent (1.2 per cent) of 'extremely' high-redshift $z > 7$ sources.

4.2.3 bSFH versus cSFH in submillimetre number counts

Here, we consider the bSFH. The difference between bSFH and cSFH is larger in submillimetre number counts than in NIR number counts, because dust accumulation makes the FIR luminosity increase efficiently while UV suffers from extinction by dust. The FIR luminosity increases by an order of magnitude as a result of the increase of star formation rate and dust content. Therefore, the effect of the bSFH can be examined by adopting an FIR luminosity 1/10 times smaller than for cSFH for $z > z_{\rm burst}$. For $z > z_{\rm burst}$, we adopt the same star formation rate as that of cSFH. As a result, the FIR luminosity rises by 10 times at $z = z_{\rm burst}$ in the bSFH. The expected submillimetre number counts for the bSFH is shown by the dashed lines in Fig. 5. A clear difference between the two scenarios cannot be seen at the ALMA detection limit. Since ALMA is not sensitive to galaxies at $z \gtrsim 7$ (Section 4.2.1), we cannot distinguish the two SFHs as long as the difference appears at $z \gtrsim 7$.

4.3 Integrated light of UV and FIR emissions

We also predict the level of the flux integrated for all the galaxies from $z_{\rm max} = 20$ to $z_{\rm min} = 5$, to see whether our model is consistent with the current observational constraints, and to compare our result with future more sensitive observations. The integrated light from all the extragalactic objects (extragalactic background radiation) has been detected in a wide range of wavelength (e.g. Hauser & Dwek 2001). We can examine what fraction of the extragalactic background light is produced by the high-redshift galaxies by using our results.

Theoretically, the intensity of integrated light produced by sources between $z_{\rm min}$ and $z_{\rm max}$ at an observed frequency ν is estimated by

$$I_\nu = \int_{z_{\rm min}}^{z_{\rm max}} {\rm d}z \int_{M_{\rm min}}^{M_{\rm max}} {\rm d}M \left[\frac{\partial n(M,z)}{\partial M} \frac{{\rm d}V(z)}{{\rm d}z} \frac{(1+z)L_{(1+z)\nu}}{4\pi d_{\rm L}^2} \right]. \quad (41)$$

The same spectra (L_ν) as Section 4.2 are adopted for both FIR and UV.

The submillimetre and NIR integrated intensities of the high-redshift galaxies are shown in Fig. 7 (thick solid lines). Both fluxes are well below the observed extragalactic background radiation. The largest ($\simeq$10 per cent) contribution of the high-redshift galaxies is expected in the millimetre range. This indicates that future ALMA

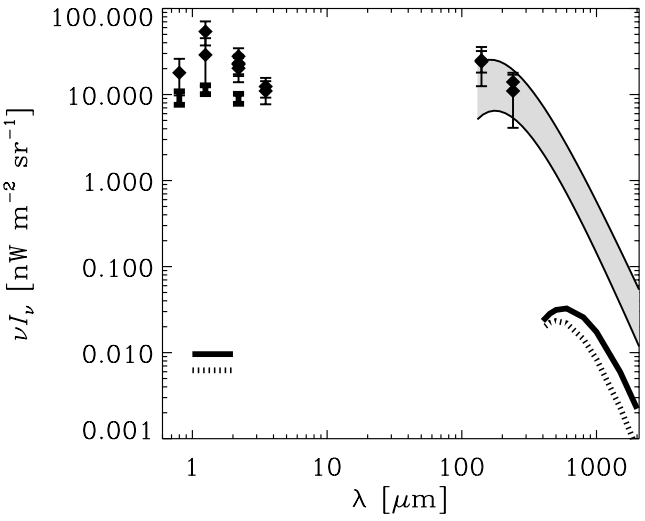

Figure 7. Predicted intensity levels of integrated light from all the high-redshift ($5 < z < 20$) galaxies for (sub)millimetre and near-infrared wavelengths (thick solid lines). The contribution from galaxies with $5 < z < 7$ is also calculated (thick dotted lines). We have also calculated the integrated light from all the high-redshift galaxies in the bSFH scenario, but the results are indistinguishable from the thick dotted lines in both UV and (sub)millimetre. The observational data for extragalactic background radiation are also shown because our predictions should lie below them. References: Berstein, Freedman & Madore (2002, 0.8 μm); Cambrési et al. (2001, 1.25 and 2.2 μm); Wright (2001, 1.25 and 2.2 μm); Gorjian, Wright & Chary (2000, 2.2 and 3.5 μm); Wright & Reese (2000, 2.2 and 3.5 μm); Hauser et al. (1998, 140 and 240 μm); Lagache et al. (2000, 140 and 240 μm). We also show the ranges estimated from integration of NIR galaxy counts by Totani et al. (2001, thick error bars without symbols). The shaded area indicates the observed level constrained by *COBE* measurement (extragalactic background; Fixsen et al. 1998).

1.3-mm observations will be the most efficient to isolate the high-redshift contribution.

In Fig. 7, we also show the integrated intensities in the case of $z_{\rm max}=7$ and $z_{\rm min}=5$ (thick dotted lines). Comparing thick solid and dotted lines, we see that roughly 52 and 35 per cent of the high-redshift ($z>5$) integrated light comes from sources with $z>7$ at millimetre and UV wavelengths, respectively. The model predictions in the case of the bSFH are also shown but the results are indistinguishable from the thick dotted lines (the difference is at most 7 per cent). Therefore, if the bSFH is correct, the integrated light from $z>5$ sources is reduced by half in the millimetre range.

For NIR, a more elaborate model focusing on Population III stars has been developed by Santos, Bromm & Kamionkowski (2002) and Salvaterra & Ferrara (2002). These authors took into account the formation of Population III stars in haloes less massive than our $M_{\rm min}$. They also considered stars whose mass is larger than 100 $\mathrm{M}_{\odot}$ because Population III stars are widely believed to be massive. Our model, on the other hand, has included $M_{\rm min}$ to exclude galaxies that cannot sustain gas against energy input from SNII, but adopted a more standard IMF. The integrated light of NIR by Santos et al. (2002) is two orders of magnitude higher than our integrated light of high-redshift galaxies, although we should note that 'extreme' conditions (star formation efficiency of 40 per cent, activation of star formation in haloes less massive than $M_{\rm min}$) are required in their paper to realize such a high value of integrated flux.

4.4 Integrated metal-line intensity

Suginohara et al. (1999) have proposed that the spatial fluctuations of integrated metal-line intensity can be used as a tracer of metal production in high-redshift sources. Now that we have analysed the metal production and the star formation history in a consistent manner, it is worth re-examining the integrated metal-line intensity within our framework.

We consider an observation that is sensitive to the frequency range $[\nu_{\rm obs}-\Delta\nu_{\rm obs}/2,\ \nu_{\rm obs}+\Delta\nu_{\rm obs}/2]$. If we are to detect a metal line whose frequency is $\nu_{\rm line}$, the redshift range that we can observe is

$$[z_1, z_2] \equiv [\nu_{\rm line}/(\nu_{\rm obs}+\Delta\nu_{\rm obs}/2)-1,\ \nu_{\rm line}/(\nu_{\rm obs}-\Delta\nu_{\rm obs}/2)-1].$$

Therefore, the integrated line intensity, $I_{\rm line}(\nu_{\rm obs};\Delta\nu_{\rm obs})$, is

$$I_{\rm line}(\nu_{\rm obs};\Delta\nu_{\rm obs}) = \int_{z_1}^{z_2} {\rm d}z \int_{M_{\rm min}}^{M_{\rm max}} {\rm d}M \left[\frac{\partial n(M,z)}{\partial M}\frac{{\rm d}V(z)}{{\rm d}z}\frac{L_{\rm line}}{4\pi d_{\rm L}^2}\right], \quad (42)$$

where we assume that $\Delta\nu$ is much wider than the linewidth of each galaxy. In this paper, we assume $z_1=5$ and $z_2=7$ to concentrate on high-redshift galaxies detected by ALMA (Section 4.2.1). Here, we again approximate (M, z) with $(M_{\rm vir}, z_{\rm vir})$. In Table 4, we show $I_{\rm line}^{\rm max}$ relative to the CMB intensity, where the superscript 'max' indicates that the integrated line intensity is calculated by using the maximum line intensity as listed in Table 3. We also present $\nu_{\rm obs}I_{\rm line}^{\rm max}$ in Table 4.

As discussed in Section 2.5.2, the metal-line intensity should be multiplied by $\mathcal{F}<1$ if the gas density of galaxies is lower than $n_{\rm H}^{\rm c}$. Adopting the mean density in Section 2.1.1, we obtain $\mathcal{F}\simeq 5.5\times10^{-2}, 9.7\times10^{-3}, 5.8\times10^{-5}, 2.9\times10^{-4}$ and 9.7×10^{-3} at $z\sim6$ (average between z_1 and z_2) for C I 609 μm, C I 370 μm, O I 63.2 μm, O I 146 μm and C II 158 μm, respectively. Hence intensities are reduced by the small $\mathcal{F}$ values and are difficult to detect. However, if we adopt, for example, the typical density for the photodissociation region in the nearby Universe $\sim10^3$ cm^{-3} (Hollenbach & McKee 1979), we obtain $\mathcal{F}\sim0.68, 0.26, 2.1\times10^{-3}$, 1.0×10^{-2} and 0.26 for C I 609 μm, C I 370 μm, O I 63.2 μm, O I 146 μm and C II 158 μm, respectively. In Fig. B1 (in Appendix B), we show $\mathcal{F}$ as a function of hydrogen number density. Observations of the integrated line intensity will constrain the typical gas density in high-redshift galaxies by comparison with theoretical maximum values listed in Table 4. If more than two metal lines are detected, a consistency check of gas density is possible.

5 SUMMARY AND DISCUSSIONS

5.1 Summary of evolutionary properties

In order to quantify the importance of dust on the first star formation activity in the Universe, we have solved the time evolution of dust mass in the galaxies formed in the redshift range $z>5$, when the age of the Universe is $\lesssim1$ Gyr. We have taken into account the importance of H_2 abundance for the star formation rate, and the formation of molecules on dust in a consistent manner (Section 2). In particular, we have made the first attempt to tie the star formation efficiency to H_2 abundance in relatively primordial environments (Section 2.2). Even when this inefficient phase of star formation is included, an active phase of star formation takes place after a few $t_{\rm cir}$ (much shorter than the Hubble time-scale) because a significant amount of dust is accumulated to activate the H_2 formation on the grain surfaces (Fig. 1). This suggests that the grains play an essential role in causing the first active phase of star formation. As a result, we have provided robust support for some theoretical works that have implicitly assumed that stars are formed at high redshift as efficiently as at low redshift.

Radiative properties of high-redshift star-forming galaxies are also predicted. We have found that a significant amount of luminosity is radiated in the FIR range. The FIR luminosity becomes comparable to the UV luminosity in a few $t_{\rm cir}$, when a significant amount of dust is accumulated (Fig. 3). This efficient reprocessing of the UV light into the FIR results partly from the dense (i.e. large optical depth) environment of high-redshift galaxies. Observations of the FIR light (submillimetre light in the observer's rest frame) as well as those of the stellar light are thus crucial to trace the whole stellar radiative energy from high-redshift galaxies.

In the framework of our model we have also given an approximate estimate of some submillimetre metal-line luminosities. However,

Table 4. Metal lines considered in this paper.

Species	m_i ($\mathrm{M}_{\odot}$)	Transition	Wavelength (μm)	$A_{{\rm u}\ell}$ (s^{-1})	$n_{\rm H}^{\rm c}$ (cm^{-3})	$I_{\rm metal}^{\rm max}/I_{\rm CMB}$	$\nu_{\rm obs}I_{\rm metal}^{\rm max}$ (n W m^{-2})
C	0.17	$^3\mathrm{P}_1\rightarrow{}^3\mathrm{P}_0$	609	7.93×10^{-8}	4.7×10^2	3.6×10^{-5}	4.3×10^{-4}
		$^3\mathrm{P}_2\rightarrow{}^3\mathrm{P}_2$	370	2.68×10^{-7}	2.8×10^3	1.5×10^{-6}	4.6×10^{-5}
O	1.2	$^3\mathrm{P}_1\rightarrow{}^3\mathrm{P}_2$	63.2	8.95×10^{-5}	4.7×10^5	11	13
		$^3\mathrm{P}_0\rightarrow{}^3\mathrm{P}_1$	146	1.70×10^{-5}	9.5×10^4	7.2×10^{-3}	0.33
C^+	0.17	$^2\mathrm{P}_{1/2}\rightarrow{}^2\mathrm{P}_{3/2}$	158	2.36×10^{-6}	2.8×10^3	1.0×10^{-4}	5.3×10^{-3}

this can only been seen as an upper limit to the actual luminosity because considerable uncertainty is present on the gas density (Section 2.5.2 and Appendix B). If future submillimetre or millimetre observations detect metal lines, a density probe of ISM of the high-redshift galaxies will be possible. If more than two types of metal lines are detected, density can be estimated more precisely.

5.2 Future observational tests

In about ten years, it will become possible to detect sources at high redshift ($z > 5$) in both submillimetre and NIR. The luminosity level of the galaxies at these wavelengths will put important constraints on our model. Therefore, we have calculated the number counts for both wavelengths. As a result, we have found that ALMA (450 μm, 850 μm and 1.3 mm bands) and *NGST* (NIR bands) can detect several times 10^3 and 10^6 high-redshift galaxies per square degree, respectively. These numbers can be used to test our model.

We have also calculated the integrated intensity of the metal-line emission from the galaxies from $z = 5$ to 7. Although a precise determination of the line intensity requires a model for the gas density [perhaps a model for photodissociation region as in Hollenbach & McKee (1979) is also necessary], we can estimate a maximum intensity for the integrated metal-line intensity. The results are listed in the last two columns of Table 4. The contamination with the cosmic submillimetre and microwave background could represent a potential problem, but such high-redshift galaxies have a correlation scale of the order of 10 arcsec (Appendix C). Therefore, a fluctuation analysis of sky brightness in the (sub)millimetre range can discriminate the metal-line signal from other contaminating sources by examining the typical correlation scale. A quantitative analysis of the fluctuations using the structure formation theory is left for future work. It may also be possible to probe the gas density of high-redshift galaxies through the factor $\mathcal{F}$ in Appendix B, if more than two kinds of metal lines are detected. The relative intensities of two lines can be used to derive a probable value of $n_{\rm H}$.

Finally, we should mention how to select high-redshift galaxies efficiently. Galaxy colours (flux ratios between two bands) are often used for the selection. We have shown that ALMA can detect galaxies at $z \lesssim 7$. The peak of the dust emission lies roughly between 500 and 800 μm for galaxies between $z = 5$ and 7. For example, 450 μm versus 1.3 mm flux ratio (450 − 1300 μm colour) gives us useful information on the redshift, because the peak of flux lies between these bands only for the high-redshift galaxies. In Fig. 8, we show the flux at 850 μm ($S_{850\ \mu\rm m}$) and 450 − 1300 μm colour ($S_{450\ \mu\rm m}/S_{1.3\,\rm mm}$) predicted by the modified blackbody spectra (equation 39). The galaxies detected by ALMA in that redshift range have typical flux levels ∼ 10–100 μJy and the 450 − 1300 μm colour is typically less than 3. In Fig. 8, we also show the ALMA detection limit (horizontal dashed line). Galaxies with $M_{\rm vir} \gtrsim 10^{11.5}\ {\rm M}_\odot$ will be detected by ALMA. At $z > 7$, however, the number of such massive galaxies is negligible and does not contribute to number counts. Typically, galaxies whose redshift is less than 4 fall to the right of the vertical dotted line (Takeuchi et al. 2001b).

We can also select high-redshift galaxies efficiently from optical observations by using the 'drop-out' technique (Steidel et al. 1996). The Lyman limit at the wavelength of 912 Å in the rest frame of a galaxy is redshifted to 5500–7300 Å for galaxies at $z = 5$–7. Therefore, optical/NIR observations of galaxies by *NGST* (Mather & Stockman 2000) or other sensitive facilities provides a way to sample the high-redshift candidates independent from the ALMA sample. A large sample of galaxies with *V*- or *R*-band drop-out should be collected by future observations. After spatial cross-identification

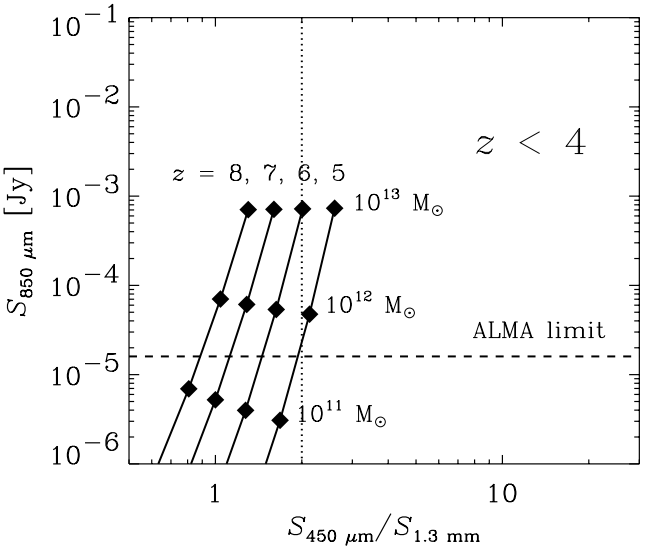

Figure 8. Relation between the flux at $\lambda = 850$ μm ($S_{850\ \mu\rm m}$) and the 450 − 1300 μm colour ($S_{450\ \mu\rm m}/S_{1.3\,\rm mm}$). [We adopt the same notation as in fig. 10 of (Takeuchi et al. 2001b) in this figure.] Our model predictions are identified by filled diamonds for $z = 5$, 6, 7 and 8 and $M_{\rm vir} = 10^{11}$, 10^{12} and 10^{13} M$_\odot$. The horizontal dashed line indicates the detection limit of ALMA. Low-redshift galaxies ($z < 4$) typically fall on the right of the vertical dotted line (Takeuchi et al. 2001b).

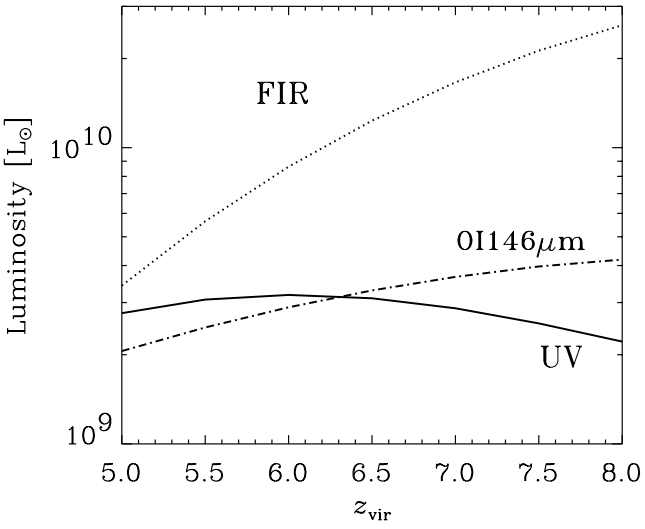

Figure 9. Luminosities as a function of formation redshift $z_{\rm vir}$ for $M_{\rm vir} = 10^{11.5}$ M$_\odot$. Such a massive galaxy will be detected by ALMA. The solid, dotted and dot-dashed lines represent ultraviolet, far-infrared and O I 146 μm (maximum; $\bar{L}^{\rm max}_{\rm O146}$) luminosities defined at four circular times.

of drop-out sample with ALMA sample, we can investigate the optical–submillimetre flux ratio as a test of our model. Galaxies with $M_{\rm vir} \gtrsim 10^{11.5}\ {\rm M}_\odot$ are detectable by both ALMA and *NGST*. In order to see the typical luminosities for galaxies detected by ALMA, we show in Fig. 9 $\bar{L}_{\rm UV}$ and $\bar{L}_{\rm FIR}$ as functions of $z_{\rm vir}$. We see that FIR/UV flux ratios are 1.2, 2.7 and 5.8 for $z_{\rm vir} = 5$, 6 and 7, respectively. In the same figure, we also present $\bar{L}^{\rm max}_{\rm O146}$. As mentioned in Section 4.4, the ratio between the observed line luminosity and $\bar{L}^{\rm max}_{\rm O146}$ (i.e. $\mathcal{F}$) can be used to estimate the density of the ISM.

5.3 Connection to lower redshift

As shown in Fig. 4, our predictions connect smoothly to the lower-redshift star formation history. Our model, however, cannot be applied to galaxy evolution at $z < 5$ because after that epoch dust is supplied from late-type stars as well as SNII. It is observationally known that mergers between giant galaxies contribute significantly to luminous infrared populations in the local Universe (Sanders & Mirabel 1996) and even at $z \sim 1$ (Roche & Eales 1999). When we apply our framework to lower redshifts, therefore, it is necessary to extend our model to include the details of the merging history of galaxies. We should note that the enhancement of molecular formation is also a key to star formation activity in mergers (e.g. Walter et al. 2002).

Recent studies using the Subaru telescope (Ouchi et al. 2002) have pushed observations as deep as $z \sim 5$. Therefore, the luminosity function (or comoving star formation rate) derived from the 'Subaru Deep Field', which is as wide as 600 arcmin^2 and as deep as 26 AB magnitude around 7000 Å, will allow us to compare our results at $z \sim 5$ directly. The luminosity function at $z \sim 5$ is also important to constrain the evolutionary scenario of Lyman break populations found at $z \sim 3$. Is the luminosity function of galaxies at $z \sim 5$ explained by the same population of Lyman break galaxies at $z \sim 3$? Recently, Ferguson, Dickinson & Papovich (2002) have given a negative answer to this question, but further studies are necessary to reveal the link between these two epochs.

We have stressed the importance of dust on the formation of a molecule-rich environment. In the lower-redshift ($z < 5$) Universe, it is observationally known that there is a correlation between the abundances of dust and molecules for DLAs (Ge et al. 2001). This strongly suggests the important role of dust for molecule formation (see also Levshakov et al. 2002). However, the correlation is not firmly assessed and a further observational sample seems to be required (Petitjean et al. 2000). Petitjean et al. also noted that most DLAs may arise selectively in warm and diffuse neutral gas. Liszt (2002) has shown that, even in a cool medium, H_2 formation can be suppressed because of low dust content and strong UV radiation field. Moreover, DLAs trace a diverse population with various masses, surface brightnesses, etc. (e.g. Pettini 2002). In spite of those complexities, DLAs are promising objects to study the link between the abundances of dust and molecules in the early Universe.

ACKNOWLEDGMENTS

We thank M. Edmunds, the referee, for helpful comments that improved this paper very much. We also thank B. Ciardi, T. T. Takeuchi and M. Ouchi for useful discussions and suggestions about various topics in galaxy evolution. Some of our cosmological results were checked against the codes provided by K. Yoshikawa. We are grateful to T. T. Ishii for helping with IDL programming. HH was supported by a JSPS Postdoctoral Fellowship for Research Abroad. We fully utilized NASA's Astrophysics Data System Abstract Service (ADS).

REFERENCES

Abel T., Anninos P., Zhang Y., Norman M. L., 1997, New Astron., 2, 181
Abel T., Bryan G. L., Norman M. L., 2002, Sci, 295, 93
Anders E., Grevesse N., 1989, Geochim. Cosmochim. Acta, 53, 197
Armus L., Matthews K., Neugebauer G., Soifer B. T., 1998, ApJ, 506, L89
Barkana R., 2002, New Astron., 7, 85
Barnes J., Efstathiou G., 1987, ApJ, 319, 575
Bernstein R. A., Freedman W. L., Madore B. F., 2002, ApJ, 571, 56
Bromm V., Coppi P. S., Larson R. B., 2002, ApJ, 564, 23
Buat V., Deharveng J. M., Donas J., 1989, A&A, 223, 42
Cambrési L., Reach W. T., Beichman C. A., Jarrett T. H., 2001, ApJ, 555, 563
Carroll S. M., Press W. H., Turner E. L., 1992, ARA&A, 30, 499
Ciardi B., Loeb A., 2000, ApJ, 540, 687
Ciardi B., Ferrara A., Governato F., Jenkins A., 2000, MNRAS, 314, 611
Cole S., Lacey C. G., Baugh C. M., Frenk C. S., 2000, MNRAS, 319, 168
Cox A. N., 2000, Allen's Astrophysical Quantities, 4th edn. Springer, New York
Dale D. A., Helou G., Neugebauer G., Soifer B. T., Frayer D. T., Condon J. J., 2001, AJ, 122, 1736
Devriendt J. E. G., Guiderdoni B., 2000, A&A, 363, 851
Draine B. T., Bertoldi F., 1996, ApJ, 468, 269
Draine B. T., Lee H. M., 1984, ApJ, 285, 89
Dwek E. et al., 1983, ApJ, 274, 168
Dwek E. et al., 1998, ApJ, 508, 106
Edmunds M. G., 2001, MNRAS, 328, 223
Elbaz D., Cesarsky C. J., Chanial P., Aussel H., Franceschini A., Fadda D., Chary R. R., 2002, A&A, 384, 848
Ferguson H. C., Dickinson M., Papovich C., 2002, ApJ, 569, L65
Ferrara A., 1998, ApJ, 499, L17
Ferrara A., Pettini M., Shchekinov Y., 2000, MNRAS, 319, 539
Fixsen D. J., Dwek E., Mather J. C., Bennett C. L., Shafer R. A., 1998, ApJ, 508, 123
Frenklach M., Feigelson E., 1997, in Pendleton Y. J., Tielens A. G. G. M., eds, ASP Conf. Ser. Vol. 122, From Stardust to Planetesimals. Astron. Soc. Pac., San Francisco, p. 107
Galli D., Palla F., 1998, A&A, 335, 403
Gardner J. P., Satyapal S., 2000, AJ, 119, 2589
Ge J., Bechtold J., Kulkarni P., 2001, ApJ, 547, L1
Gehrz R. D., 1989, in Allamandola L. J., Tielens A. G. G. M., eds, Proc. IAU Symp. 135, Interstellar Dust. Kluwer, Dordrecht, p. 445
Gispert R., Lagache G., Puget J. L., 2000, A&A, 360, 1
Gorjian V., Wright E. L., Chary R. R., 2000, ApJ, 536, 550
Granato G. L., Lacey C. G., Silva L., Bressan A., Baugh C. M., Cole S., Frenk C. S., 2000, ApJ, 542, 710
Haiman Z., Rees M. J., Loeb A., 1996, ApJ, 467, 522
Hauser M. G., Dwek E., 2001, ARA&A, 39, 249
Hauser M. G. et al., 1998, ApJ, 508, 25
Hirashita H., Hunt L. K., Ferrara A., 2002a, MNRAS, 330, L19
Hirashita H., Tajiri Y. Y., Kamaya H., 2002b, A&A, 388, 439
Hollenbach D. J., McKee C. F., 1979, ApJS, 41, 555
Hu E. M., Cowie L. L., McMahon R. J., Capak P., Iwamuro F., Kneib J.-P., Maihara T., Motohara K., 2002, ApJ, 568, L75
Hutchings R. M., Santoro F., Thomas P. A., Couchman H. M. P., 2002, MNRAS, 330, 927
Ikeuchi S., 1988, Fundam. Cosmic Phys., 12, 255
Inoue A. K., Hirashita H., Kamaya H., 2000, AJ, 120, 2415
Jones A. P., Tielens A. G. G. M., Hollenbach D. J., 1996, ApJ, 469, 740
Kamaya H., Silk J., 2002, MNRAS, 332, 251
Katz N., Furman I., Biham O., Pirronello V., Vidali G., 1999, ApJ, 522, 305
Kauffmann G., Charlot S., 1998, MNRAS, 294, 705
Kennicutt R. C., Jr, 1998, ApJ, 498, 541
Kitayama T., Ikeuchi S., 2000, ApJ, 529, 615
Kitayama T., Suto Y., 1996, ApJ, 469, 480
Kitayama T., Susa H., Umemura M., Ikeuchi S., 2001, MNRAS, 326, 1353
Kozasa T., Hasegawa W., Nomoto K., 1991, A&A, 249, 474
Lagache G., Haffner L. M., Reynolds R. J., Tufte S. L., 2000, A&A, 354, 247
Levshakov S. A., Dessauges-Zavadsky M., D'Odorico S., Molaro P., 2002, ApJ, 565, 696
Lisenfeld U., Ferrara A., 1998, ApJ, 496, 145
Liszt H., 2002, A&A, 389, 393
McKee C. F., 1989, in Allamandola L. J., Tielens A. G. G. M., eds, Proc. IAU Symp. 135, Interstellar Dust. Kluwer, Dordrecht, p. 431
McKee C. F., Ostriker J. P., 1977, ApJ, 218, 148

Madau P., Ferguson H. C., Dickinson M., Giavalisco M., Steidel C. C., Fruchter A., 1996, MNRAS, 283, 1388
Madau P., Pozzetti L., Dickinson M., 1998, ApJ, 498, 106
Madau P., Ferrara A., Rees M. J., 2001, ApJ, 555, 92
Malkan M. A., Stecker F. W., 2001, ApJ, 555, 641
Mather J. C., Stockman H. S., 2000, in Matsumoto T., Shibai H., eds, ISAS Rep. SP No. 14, Mid- and Far-Infrared Astronomy and Future Space Missions. Sagamihara, Institute of Space and Astronautical Science, p. 203
Matsuda T., Sato H., Takeda H., 1969, Prog. Theor. Phys., 42, 219
Mo H. J., White S. D. M., 2002, MNRAS, 336, 112
Moseley S. H., Dwek E., Glaccum W., Graham J. R., Loewenstein R. F., Silverberg R. F., 1989, Nat, 340, 697
Nagashima M., Totani T., Gouda N., Yoshii Y., 2001, ApJ, 557, 505
Nakamura F., Umemura M., 2002, ApJ, 569, 549
Nishi R., Susa H., 1999, ApJ, 523, L103
Norman C. A., Spaans M., 1996, ApJ, 480, 145
Oh S. P., 2002, MNRAS, submitted
Omukai K., 2000, ApJ, 534, 809
Omukai K., Nishi R., 1998, ApJ, 508, 141
Ouchi M. et al., 2002, ApJ, in press (astro-ph/0202204)
Partridge R. B., Peebles P. J. E., 1967, ApJ, 148, 377
Pearson C. P., 2001, MNRAS, 325, 1511
Peebles P. J. E., 1980, The Large Scale Structure of the Universe. Princeton Univ. Press, Princeton, NJ
Pei Y. C., Fall S. M., Hauser M. G., 1999, ApJ, 522, 604
Petitjean P., Srianand R., Ledoux C., 2000, A&A, 364, L26
Pettini M., 2002, in Felet R., et al., eds, 17th IAP Astrophysics Colloquium, Gaseous Matter in Galaxies and Intergalactic Space. Frontier Group, Paris, p. 315
Press W. H., Schechter P., 1974, ApJ, 187, 425
Puget J.-L., Abergel A., Bernard J.-P., Boulanger F., Burton W. B., Désert F.-X., Hartmann D., 1996, A&A, 308, L5
Rana N. C., Wilkinson D. A., 1986, MNRAS, 218, 497
Ripamonti E., Haardt F., Ferrara A., Colpi M., 2002, MNRAS, 334, 401
Roche N., Eales S. A., 1999, MNRAS, 307, 111
Salvaterra R., Ferrara A., 2002, MNRAS, submitted
Sanders D. B., Mirabel I. F., 1996, ARA&A, 34, 749
Santos M. R., Bromm V., Kamionkowski M., 2002, MNRAS, in press (astro-ph/0111467)
Schaerer D., 2002, A&A, 382, 28
Shanks T., Metcalfe N., Fong D., McCracken H., Campos A., Thompson D., 2001, in Harwit M., Hauser M. G., eds, Proc. IAU Symp. 204, The Extragalactic Infrared Background and its Cosmological Implications. Astron. Soc. Pac., San Francisco, p. 347
Shapiro P., Kang H., 1987, ApJ, 318, 32
Smail I., Ivison R. J., Blain A. W., Kneib J.-P., 1998, ApJ, 507, L21
Soifer B. T., Neugebauer G., Franx M., Matthews K., Illingworth G. D., 1998, ApJ, 501, L171
Somerville S. R., Primack J. R., 1999, MNRAS, 310, 1087
Spitzer L., Jr, 1978, Physical Processes in the Interstellar Medium. Wiley, New York
Steidel C. C., Giavalisco M., Pettini M., Dickinson M., Adelberger K. L., 1996, ApJ, 462, L17
Steidel C. C., Adelberger K. L., Giavalisco M., Dickinson M., Pettini M., 1999, ApJ, 519, 1
Steinmetz M., Bartelmann M., 1995, MNRAS, 272, 570
Suginohara M., Suginohara T., Spergel D. N., 1999, ApJ, 512, 547
Takeuchi T. T., Ishii T. T., Hirashita H., Yoshikawa K., Matsuhara H., Kawara K., Okuda H., 2001a, PASJ, 53, 37
Takeuchi T. T., Kawabe R., Kohno K., Nakanishi K., Ishii T. T., Hirashita H., Yoshikawa K., 2001b, PASP, 113, 586
Tan J. C., Silk J., Balland C., 1999, ApJ, 522, 579
Tegmark M., Silk J., Rees M. J., Blanchard A., Abel T., Palla F., 1997, ApJ, 474, 1
Tielens A. G. G. M., Hollenbach D., 1985, ApJ, 291, 722
Tinsley B. M., 1980, Fundam. Cosmic Phys., 5, 287
Tinsley B. M., Danly L., 1980, ApJ, 242, 435
Todini P., Ferrara A., 2001, MNRAS, 325, 726
Tosi M., Diaz A. I., 1990, MNRAS, 246, 616
Totani T., Takeuchi T. T., 2002, ApJ, 570, 470
Totani T., Yoshii Y., Iwamuro F., Maihara T., Motohara K., 2001, ApJ, 550, L137
Walter F., Weiss A., Martin C., Scoville N., 2002, AJ, 123, 225
White S. D. M., Frenk C. S., 1991, ApJ, 379, 52
Wilson C. D., Scoville N., Madden S. C., Charmandaris V., 2000, ApJ, 542, 120
Woosley S. E., Weaver T. A., 1995, ApJS, 101, 181
Wright E. L., 2001, ApJ, 553, 538
Wright E. L., Reese E. D., 2000, ApJ, 545, 53
Xu C., Lonsdale C. J., Shupe D. L., O'Linger, J., Masci F., 2001, ApJ, 562, 179

APPENDIX A: H_2 FORMATION ON GRAINS

The production rate of molecular fraction via dust surface reaction is estimated as (Hollenbach & McKee 1979)

$$\left[\frac{\mathrm{d}f_{\mathrm{H_2}}}{\mathrm{d}t}\right]_{\mathrm{dust}} = f_0 n_{\mathrm{dust}} \pi a^2 \bar{v} S, \tag{A1}$$

where $f_{\mathrm{H_2}}$ is the molecular fraction of hydrogen (equation 1), f_0 is the neutral fraction of hydrogen, n_{H} is the number density of hydrogen nuclei, $\bar{v}$ is the mean thermal speed of hydrogen, n_{dust} is the number density of dust grains, a is the radius of a grain (spherical grains with a single radius are assumed) and S is the sticking efficiency of hydrogen atoms. The thermal speed is given by (Spitzer 1978)

$$\bar{v} = \sqrt{\frac{8}{\pi}\frac{k_{\mathrm{B}}T}{m_{\mathrm{H}}}} = 1.4 \times 10^5 \left(\frac{T}{100\,\mathrm{K}}\right)^{1/2} \mathrm{cm\,s^{-1}}, \tag{A2}$$

where k_{B} is the Boltzmann constant, T is the gas temperature and m_{H} is the mass of a hydrogen atom. Here, we define the reaction rate of the H_2 formation on grains, R_{dust}, as

$$R_{\mathrm{dust}} \equiv \frac{3 m_{\mathrm{H}} \bar{v} S}{8 a \delta} = 1.4 \times 10^{-14} S \left(\frac{T}{100\,\mathrm{K}}\right)^{1/2} \left(\frac{a}{0.03\,\mu\mathrm{m}}\right)^{-1} \times \left(\frac{\delta}{2\,\mathrm{g\,cm^{-3}}}\right)^{-1} \mathrm{cm^3\,s^{-1}}, \tag{A3}$$

where δ is the mass density of a grain. The dust-to-gas mass ratio $\mathcal{D}$ can be estimated as

$$\mathcal{D} = \frac{4\pi a^3 \delta n_{\mathrm{dust}}}{3 n_{\mathrm{H}} m_{\mathrm{H}}}. \tag{A4}$$

Using R_{dust} and $\mathcal{D}$, the right-hand side of equation (A1) becomes the second term of equation (10). We take $a = 0.03$ μm (Todini & Ferrara 2001). The sticking coefficient S is uncertain. For simplicity, we adopt $S \sim 0.2$, the value for the gas temperature when star formation occurs ($T < 300$ K) (Hollenbach & McKee 1979). When $T > 300$ K, S is assumed to be zero. The sticking efficiency of Hollenbach & McKee (1979) indicates that the dependence of S on dust temperature is negligible as long as the dust temperature, T_{dust}, is less than ∼75 K.

APPENDIX B: SIMPLE PRESCRIPTION TO INCLUDE THE LOW-DENSITY EFFECT ON LINE INTENSITY

Here we describe a simple approximate treatment to calculate FIR–submillimetre metal-line intensities. Our formula given here is appropriate for a one-zone treatment such as our model. A more accurate treatment requires detailed modelling of photodissociation regions (Hollenbach & McKee 1979; Tielens & Hollenbach 1985).

We consider a population with two energy levels (the upper and the lower are labelled as 'u' and 'ℓ', respectively). We consider a spontaneous transition, whose Einstein coefficient is denoted as $A_{u\ell}$, and collisional excitation by species whose number density is n (the collisional excitation rate is expressed as $\gamma_{\ell u}n$) and collisional de-excitation by the same species (the collisional de-excitation rate is expressed as $\gamma_{u\ell}n$). Assuming the equilibrium between the transition from u to ℓ and that from ℓ to u, the fraction of the population in the upper level, f_u, is estimated to be

$$f_u = \frac{\gamma_{\ell u} n}{A_{u\ell} + (\gamma_{u\ell} + \gamma_{\ell u})n}. \tag{B1}$$

If the collisional excitation (or de-excitation) occurs on a shorter time-scale than the spontaneous emission, the fraction in the upper level is

$$f_u^0 = \frac{\gamma_{\ell u}}{\gamma_{u\ell} + \gamma_{\ell u}}. \tag{B2}$$

Because of the spontaneous emission, the fraction in the upper level is reduced by the factor $\mathcal{F} \equiv f_u/f_u^0$. For the excitation coefficients, the following relation holds (Spitzer 1978):

$$\frac{\gamma_{\ell u}}{\gamma_{u\ell}} = \frac{g_u}{g_\ell} \exp\left(-\frac{E_{u\ell}}{k_B T_{ex}}\right), \tag{B3}$$

where g_u and g_ℓ are statistical weights for the lower and upper levels, respectively, $E_{u\ell}$ is the energy gap between the two states, k_B is the Boltzmann constant, and T_{ex} is the excitation temperature of the colliding species. In this paper, we consider metal lines whose $\gamma_{\ell u}/\gamma_{u\ell}$ is of the order of unity (i.e. $E_{u\ell} \lesssim k_B T_{ex}$) and whose exciting species is hydrogen ($n \sim n_H$). For the metal lines of interest, we finally find that

$$\mathcal{F} \sim \frac{n_H}{n_H^c + n_H} \tag{B4}$$

gives a good approximation (correct within a factor of $\sim$2), where n_{cr} is the critical density defined as

$$n_H^c \equiv \frac{A_{u\ell}}{\gamma_{u\ell}}. \tag{B5}$$

The line intensity is expected to be $\sim L_{line}^{max}$ (Section 2.5.2) if n_H is higher than n_H^c (i.e. $\mathcal{F} \sim 1$). On the contrary, if the density if much smaller than n_H^c, the line intensity is quite reduced (i.e. $\mathcal{F} \ll 1$).

In Fig. B1, we show $\mathcal{F}$ as a function of n_H, where equation (B1) is applied. If we detect the line emission intensity of high-redshift galaxies, we can make a rough estimate of the gas density by comparing the observed line intensity with L_{line}^{max}. The line ratio between two types of lines can also constrain the gas density.

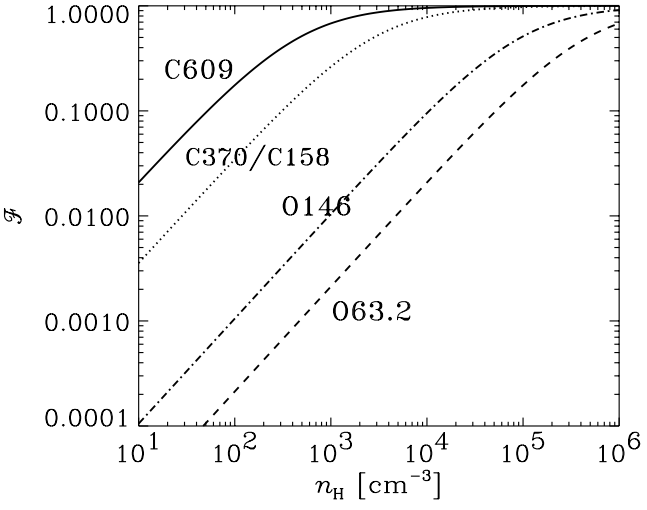

Figure B1. Reduction factor $\mathcal{F}$ to the maximum luminosity L_{line}^{max} of metal lines as a function of the number density of hydrogen atoms, n_H. The solid, dotted, dashed and dot-dashed lines represent $\mathcal{F}$ of C I 609 μm, C I 370 μm, O I 63.2 μm and O I 146 μm, respectively. Since the critical density of C II 158 μm is the same as that of C I 370 μm, $\mathcal{F}$ of C II 158 μm is represented by the dotted line. If the number density n_H is known, we can obtain the line intensity as $\mathcal{F}L_{line}^{max}$. Inversely, if we obtain $\mathcal{F}$ by comparing observed line luminosity and theoretical L_{line}^{max}, we can estimate n_H.

APPENDIX C: TYPICAL ANGULAR SIZE OF CLUSTERING

The integrated light from galaxies should trace their spatial fluctuation produced by gravitational clustering. Therefore, if we measure the typical correlation angular scale of the integrated light, we can test if the integrated light really comes from galaxies. Here, we calculate the typical correlation angular size of galaxies at a certain redshift.

The typical mass within a clustered region, M_{cl}, is estimated to be the mass scale corresponding to $\sigma(M_{cl})D(z) = 1$, where $D(z)$ is the growth factor of perturbations [$D(0) = 1$], and $\sigma(M)$ is the variance of density field smoothed with mass scale M. In this relation, M_{cl} corresponds to the mass scale at the break of the Press–Schechter mass function. We adopt $\sigma(M)$ given in the appendix of Kitayama & Suto (1996). Once M_{cl} is obtained, we can estimate the typical diameter of gravitationally clustered region, D_{cl}, as

$$D_{cl} = 2\left[\frac{3M_{cl}}{4\pi\rho_{c0}\Omega_M(1+z)^3}\right]^{1/3}, \tag{C1}$$

where ρ_{c0} is the critical density of the Universe at $z = 0$ (i.e, $\rho_{c0}\Omega_M$ is the mean mass density of the Universe at $z = 0$).

In this paper, we are particularly interested in $z \sim 6$. Using $D(6) = 0.21$, we obtain $M_{cl} = 2 \times 10^{10}\,M_\odot$ for the cosmology assumed in this paper. This corresponds to the typical comoving size of 0.33 Mpc (i.e. $D_{cl} = 0.05$ Mpc). This corresponds to an angular scale of 10 arcsec.

This paper has been typeset from a TEX/LATEX file prepared by the author.